Applied Mathematical Modelling 131 (2024) 737–763

Contents lists available at ScienceDirect

Applied Mathematical Modelling

journal homepage: www.elsevier.com/locate/apm

Equivalent micropolar model for porous guided bone regeneration mesh: Optimum design for desired mechanical properties

A. Rezaei [a], R. Izadi [a], N. Fantuzzi [b,*]

[a] DISG Department, Sapienza University of Rome, Italy
[b] DICAM Department, University of Bologna, Italy

ARTICLE INFO

Keywords:
Guided Bone Regeneration
Cosserat continua
Finite element analysis
Equivalent porous-cellular materials

ABSTRACT

In the present work, a micropolar continuum model is adopted to homogenise a heterogeneous porous model of Guided Bone Regeneration (GBR) meshes. GBR meshes are used in dentistry as mechanical barriers to isolate and protect the area of bone loss from the surrounding tissue while allowing new bone growth. The mechanical constants of the continuum are derived based on the strain energy equivalence of a periodic porous plate with its equivalent ortho-tetragonal micropolar model under prescribed boundary conditions. The effects of various architectural features such as pore shapes, patterns and sizes on the material parameters are investigated. The results show that the micropolar theory provides a better prediction of the response of the 2D porous geometries considered for the GBR mesh, compared to the classical Cauchy theory. The collected equivalent material parameters are further used for GBR mesh design, considering both mechanical and biomedical requirements. As an example, different materials and arrangements are analysed to find micropolar constitutive parameters that are comparable to bone parameters reported in the literature. This allows the GBR mesh to possess the mechanical performance that matches the adjacent bones.

1. Introduction

The use of Guided Bone Regeneration (GBR) mesh in dentistry is becoming increasingly popular. This technique uses a mechanical barrier, such as a membrane, to separate and protect the area of bone loss from the surrounding tissue so that new bone can grow in the designated area. GBR is reported to provide the best and most predictable results when used to fill peri-implant bone defects with new bone. Research in the field of GBR is still ongoing, with evidence coming mainly from preclinical studies [1]. While various types of barriers have been used in GBR, the design and mechanical properties of the GBR mesh can greatly influence its effectiveness in promoting bone growth [2].

GBR meshes have different mechanisms to fulfil their bone regenerating function. Biologically, the soft tissue of the gingiva has a high tendency to proliferate, which can fill and replace the cavity caused by the bone loss. The aim of GBR is to shield the soft tissue from the bone defect with a barrier membrane, creating a relatively closed space that promotes the multiplication of bone cells. In addition, the space provided by the GBR mesh stores bone grafts and stimulating substances that induce the adjacent bone to produce new bone cells [2–4].

On the other hand, the mechanical shielding provided by the GBR mesh determines the morphology and boundary of the

* Corresponding author.
E-mail address: nicholas.fantuzzi@unibo.it (N. Fantuzzi).

https://doi.org/10.1016/j.apm.2024.04.008
Received 24 November 2023; Received in revised form 14 March 2024; Accepted 4 April 2024
Available online 6 April 2024
0307-904X/© 2024 The Author(s). Published by Elsevier Inc. This is an open access article under the CC BY-NC-ND license (http://creativecommons.org/licenses/by-nc-nd/4.0/).

regenerated bone. It also provides sufficient stiffness to bear the chewing pressure load and thus prevent undesired deformation of the newly regenerated bone cells [4].

To create a stable bone regeneration environment, an "ideal" barrier membrane must fulfil five basic principles [2,5]:

1. Biocompatibility.
2. Space preservation requiring sufficient stiffness to maintain the space and withstand the pressure of masticatory forces.
3. Permeability or occlusivity which requires adequate porosity.
4. Tissue integration to embedding in the surrounding host tissues.
5. Clinical manipulation for ease of use and handling.

As a first expectation, the membrane should have adequate stiffness to create and maintain a suitable space for the intended osseous regeneration. On the other hand, barrier occlusivity of a membrane may be at least as important as its space-maintaining properties in the regeneration of bone defects [6]. Appropriate pore size is reported to play a role in desirable occlusivity of GBR membrane [7,8]. The architecture of the porous structure in general, rather than just the type of material used, has been suggested to confer the biological activity of a material. The membrane pores facilitate the diffusion of fluids, oxygen, nutrients, and bioactive substances for cell growth, which is essential for bone and soft tissue regeneration while nonporous barrier membranes may delay bone regeneration [2].

However, there are some biomedical aspects of the porosity that remain controversial [9]: larger pore sizes will allow faster-growing cells to overpopulate the defect space and inhibit the infiltration and activity of bone-forming cells. They can also provide an easy pathway for bacterial contamination. On the other hand, if pores are too small, cell migration of all cells is restricted. A large pore size inevitably reduces the resulting surface area of the material, which could limit the important initial steps of cell adhesion onto the membrane [1]. Overall, a compromise must be found between porosity and stiffness when designing a GBR mesh. Biologically, higher porosity facilitates the diffusion of nutrients that promote cell growth, while mechanically, higher porosity reduces the stiffness and load-bearing capacity of the GBR. Therefore, the optimal mesh design should be a mechanically robust structure that also fulfils the biomedical requirements.

Due to the latest achievements in additive manufacturing, precise microstructures with architectural features can be fabricated through 3D printing. Accordingly, precise, and individualised 3D scaffolds with a customizable pore size, pore density, and fully controlled architecture can be fabricated conveniently and quickly. The characteristics and performance of such barrier membranes can be optimized by adjusting their microstructures, given that their thickness, pore size, pore geometry and pattern affect their mechanical performance and are directly related to bone formation ability. Engineering modelling and simulation tools such as the finite element method can be used to optimise the design of the GBR mesh which can be further verified or adapted through clinical trials to meet biological requirements.

To account for microporosity, macroporosity or a combination thereof in the design of the GBR mesh, the material can be treated as a heterogeneous medium with designed porous and architected cellular structure [10,11]. On the other hand, direct modelling and discretisation of such cellular materials can lead to cumbersome computations, necessitating the definition of equivalent constitutive laws that take microscopic properties into account. The mechanical behaviour of these materials can be analysed through two approaches: detailed discrete computation and equivalent continuum approximation, thorough homogenization theories based on the selection of a Representative Volume Element (RVE) of the material [12]. The discrete analysis, using analytical approaches [13] or numerical methods like FEM, needs great computational efforts [14]. Thus, an alternative regarding their effective mechanical properties have attracted significant attention [15]. Those effective properties can be predicted by computational methods [16] to define an equivalent continuum that properly considers the influence of the microstructure on the macro-scale behaviour with reference to shape, size, and texture of lower scale features [17,18].

Since classical continuum theory cannot account for the internal length scale of cellular solids [12], non-classical (non-local [19]) continuum theories [20] that simultaneously use field description at the coarse level and preserve the memory of the material underlying structure at the fine level, can overcome this limitation [21,22]. Non-classical theories can have different attitudes in retaining more information on the material's internal structure. One approach, such as [23–25], use the primal field of classical elasticity, yet the governing equation of motions contain non-local operators. Another approach is to account for the material's heterogeneity indirectly by considering extra degrees of freedom. Among non-classical theories belonging to the second approach, elastic micropolar (Cosserat) theory [26,27], has been successfully used in many applications [14,28] to describe heterogeneous materials [29,30], such as porous materials [31–35], cellular materials [36], composites [37–39], lattices [40] and foams [41–43] and even nanostructures [21,44]. In micropolar theory, in addition to the standard displacement, the rotation of the material point is introduced, which is called microrotation to be distinguished from macro-rotation (local rigid rotation). Also, a simplified version of micropolar theory, known as couple stress theory [45], were implemented for studying porous and functionally graded porous materials [46,47].

As some examples of work related to biomedical applications, micropolar models of bone were constructed in [48,49] to investigate microstructure-related scale effects on macroscopic effective properties. Lakes and co-workers [50–54], also conducted a series of experiments and studies on bones and found that micropolar theory provides better predictions of bone response than Cauchy elasticity. Furthermore, in [55] the authors determined the micropolar elastic constants of bone using micromechanical analyses. It was assumed that bone tissue is an isotropic Cauchy-type elastic material at the microscopic level, while bone behaves as a homogeneous micropolar continuum at the macroscopic level. The effective elastic constants for the micropolar continuum were determined from the response of a bone sample. Knowing the mechanical properties of bone and considering the correct model, are of great importance for the development and use of prostheses that replace a bone or part of a bone, or in our case for GBR meshes that can perform better if

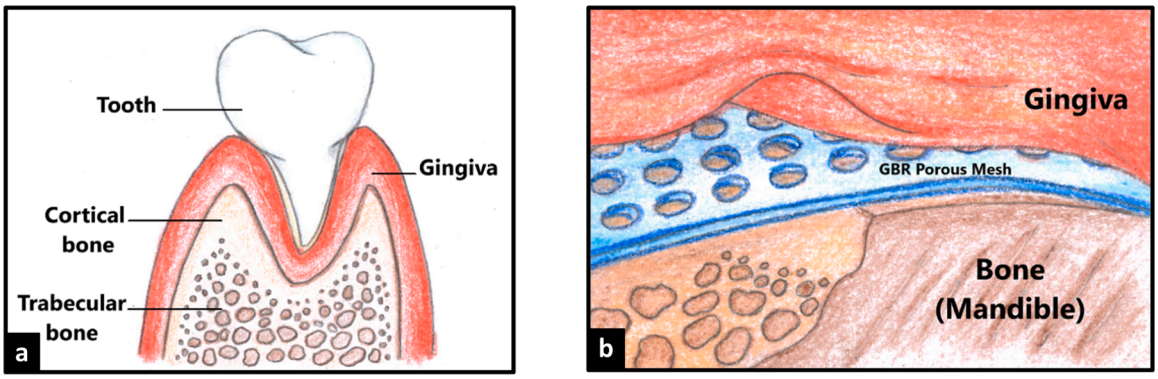

Fig. 1. a. Anatomy of the tooth and components of alveolar bone **b.** Use of a porous GBR mesh.

they have a mechanical behaviour like bone. Generally, there are three main approaches to determine equivalent micropolar parameters. Experimental, where mechanical tests such as 3-point bending, torsion or vibration are conducted to measure the material response [53,56]. Analytical, in which mathematical models are developed to calculate the parameters based on the known material microstructure [57]. Numerical, in which by implementing finite element models, the parameters are determined from the response of various loading conditions on a detailed model [29].

In the current work, we highlight the advantages of micropolar elasticity description, in the design of dental GBR meshes as porous-cellular materials. The micropolar continuum is used to homogenise the heterogeneous porous model. The mechanical constants of the continuum are derived based on the strain energy equivalence of periodic porous plates with their equivalent ortho-tetragonal micropolar model under prescribed boundary conditions. The detailed porous structure and the equivalent micropolar model are simulated by the finite element method where the latter is developed using the PDE interface of COMSOL Multiphysics software. Through a parametric study, the effects of various architectural features such as pore shapes, patterns and sizes on the material parameters are investigated. The results show that the micropolar theory provides a better prediction of the response of the 2D porous geometries with significant pore size compared to the classical Cauchy theory.

The developed mechanical model can provide a useful framework for GBR mesh design, considering both mechanical and biomedical requirements. As an example, we have investigated different materials and arrangements to find micropolar constitutive parameters that are comparable to bone parameters reported in the literature. This allows the GBR mesh to possess the mechanical performance that matches the adjacent bones.

The alveolar bone is that part of the lower jaw (mandible) and upper jaw (maxilla) which supports the teeth. It consists of two layers of compact (cortical) bone and spongy (trabecular) bone (Fig. 1a). In some areas, the alveolar bone is thin and has almost no spongy bone [58,59].

As can be seen in Fig. 1**b**, the GBR mesh is in contact with the cortical (compact) bone. To seek an optimal mechanical behavior, we try to make the material parameters of the GBR mesh consistent with its adjacent bone and suggest matching the mechanical properties of the mesh with the cortical type of the bone.

The paper is structured as follows: Section 2 presents details of the homogenisation procedure and the equivalent continuum model considered. It also gives a brief description of micropolar theory and introduces the geometric model for representing GBR meshes. The details of numerical implementation of the micropolar model using the PDE interface and FEM simulations are provided in Section 3. After, in Section 4 the results of the parametric study and the homogenisation of the 2D porous geometries are presented. This section also discusses the results and applicability of the proposed method to find GBR geometries with material parameters like bones. Finally concluding remarks are summarized in Section 5.

2. Equivalent continuum model for 2D GBR mesh

To develop a numerically efficient method for modelling the 2D porous GBR meshes with different microstructures (pores patterns), a multiscale approach is proposed in which an equivalent homogenised material represents the detailed heterogeneous structure. The equivalent material is described in the framework of micropolar theory. In this section, we first address the geometric model for representing GBR meshes and then describe the procedure to determine equivalent micropolar parameters for porous 2D plates.

2.1. Parametrization of 2D GBR mesh model

Currently, there are several types of GBR meshes available on the market (Fig. 2**a**). A common type that is widely used in dentistry is the titanium alloy (Ti6Al4V) [60] sheets with a perforated structure. Before implantation of the GBR, the required dimensions and overall shape are cut and formed by the surgeon (Fig. 2**b**).

In the current work, GBR meshed are considered as a 2D square plates with overall side length of L_{sheet} where pores are distributed regularly. The pores can be modelled with various shape and size and with different spacing which leads to different pore densities.

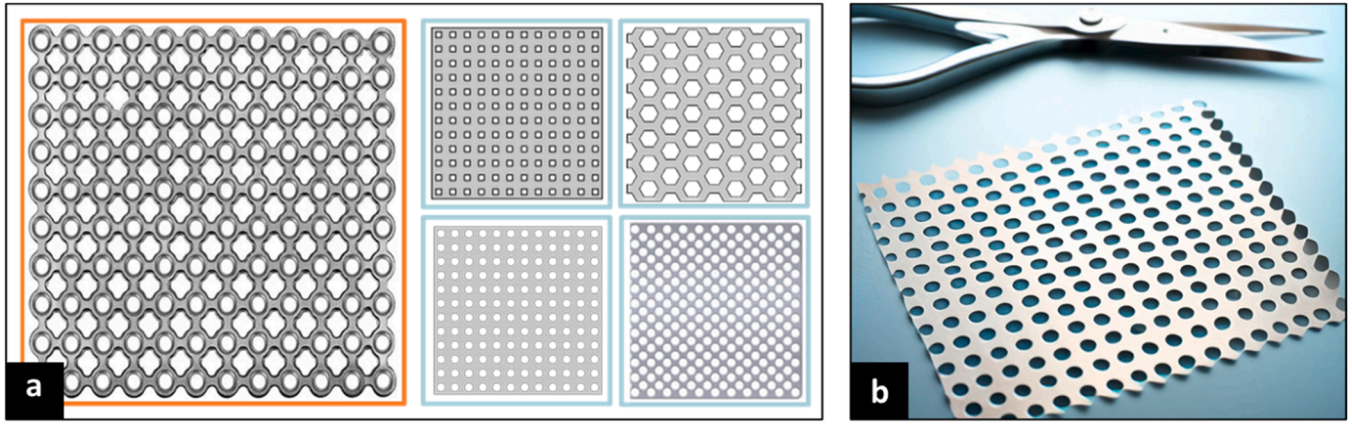

Fig. 2. **a.** Perforated titanium sheets with different patterns **b.** The required dimensions and overall shape are cut and formed by the surgeon.

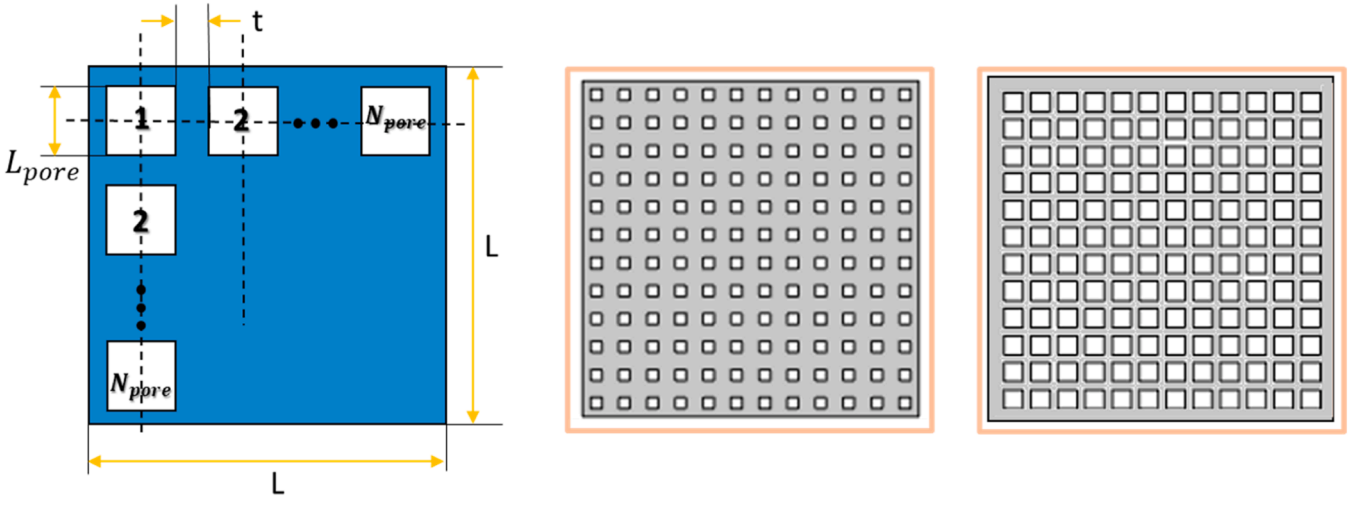

Fig. 3. A parametrized GBR sheet with rectangular shape pores.

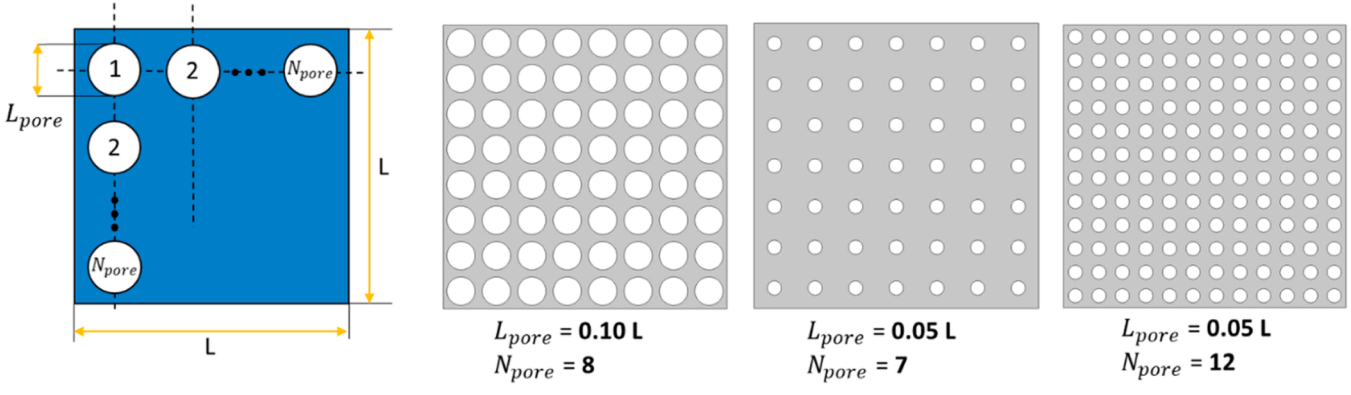

Fig. 4. The parametrization used for GBR mesh with circular pores.

Here, the pores' geometry and pattern are parametrized by two variables, the pore size (named 'L_{pore}') and the number of pores ('N_{pore}') in a row. Accordingly, wall thickness (t) will be a dependent variable and calculated as:

$$t = \frac{L_{sheet}}{N_{pore}} - L_{pore} \tag{1}$$

A parametrized GBR sheet with rectangular shape pores is shown in Fig. 3 as an example.

One of the most common patterns for GBR porous titanium mesh that are already available on the market, is the one with regular circular pores. This pattern can be parametrized using pore diameter as the indicator of pore size (L_{pore}) and the number of pores (N_{pore}) as a measurement of pore density (Fig. 4).

2.2. Multiscale homogenisation procedure

For the determination of the constitutive parameters of the equivalent model, the primary hypothesis is that the strain energy stored in the detailed structure (micro-level) under prescribed boundary conditions is equal to that of the equivalent continuum description (macro-level). In the current work, two different continua are used to describe the material at the macro- and micro-levels. At the macro-level, the micropolar continuum is chosen as it has been shown to be very suitable to describe materials with internal structures, while at the micro-level the classical Cauchy continuum is used.

2.3. Micropolar theory

In the micropolar theory, in addition to the standard displacement, the material particles that comprise the continuum are endowed with an additional degree of freedom as microrotation, which leads to the following linearized kinematic equations:

$$\begin{aligned} \varepsilon_{ij} &= u_{i,j} + e_{ijk}\phi_k \\ \mu_{kj} &= \phi_{k,j} \end{aligned} \tag{2}$$

Where u_i and ϕ_k stand for the components of displacement and micro-rotation vectors, ε_{ij} and μ_{kj} denote the components of strain and curvature tensors with e_{ijk} being the usual third order permutation symbol.

If body forces (p_i) and body couples (q_k) are also considered, the equilibrium equations take the following form:

$$\begin{aligned} \sigma_{ij,j} + p_i &= 0 \\ \mu_{kj,j} - e_{ijk}\sigma_{ij} + q_k &= 0 \end{aligned} \tag{3}$$

Where σ_{ij} and μ_{kj} are the components of the non-symmetric stress and couple-stress tensors, respectively.

Here, we consider 2D plane stress formulations to model GBR sheets. In the linearized 2D framework of micropolar, there are two displacements and one rotational component, so the generalized displacements will be:

$$\boldsymbol{u}^T = [\, u \quad v \quad \phi \,] \tag{4}$$

and the strain vector is:

$$\boldsymbol{\varepsilon}^T = [\, \varepsilon_{11} \quad \varepsilon_{22} \quad \varepsilon_{12} \quad \varepsilon_{21} \quad \kappa_1 \quad \kappa_2 \,] \tag{5}$$

where ε_{11}, ε_{22}, ε_{12}, ε_{21} are the in-plane normal and shear strains and κ_1,κ_2 are the micropolar curvatures. Note that the strain components are no longer symmetric $\varepsilon_{12} \neq \varepsilon_{21}$ in the micropolar theory.

The stress vector is also represented as:

$$\boldsymbol{\sigma}^T = [\, \sigma_{11} \quad \sigma_{22} \quad \sigma_{12} \quad \sigma_{21} \quad \mu_1 \quad \mu_2 \,] \tag{6}$$

where σ_{ij} ($i, j = 1, 2$) represents the normal ($i = j$) and shear stress ($i \neq j$) components and μ_1, μ_2 are the micro-couples. In micropolar theory, the stress components are not reciprocal, $\sigma_{12} \neq \sigma_{21}$ and the couple stress components μ_1, μ_2 must be introduced to satisfy the moment equilibrium of the micropolar body.

The micropolar anisotropic constitutive equations can be represented as:

$$\boldsymbol{\sigma} = \mathbf{C}\boldsymbol{\varepsilon} \tag{7}$$

Where $\mathbf{C}$ is the constitutive stiffness matrix. Due to hyper-elasticity, the constitutive matrix $\mathbf{C}$ is symmetrical [61]. This matrix is obtained by an energetic homogenisation technique presented in [62].

The geometries considered here for porous GBR mesh are symmetric with respect to a 90° rotation. These symmetries in the 2D model, implies a special kind of orthotropic material named as "ortho-tetragonal" [38]. In such material model, some constitutive perceptions exist that are presented in [62]. The constitutive equations for these materials can be presented in Voigt's notation as:

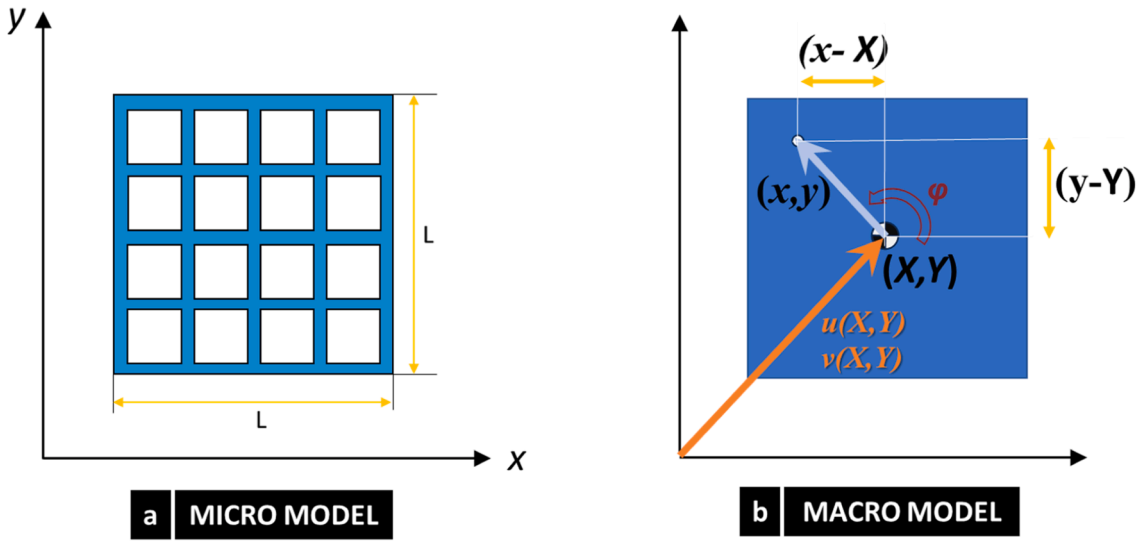

Fig. 5. RVE Geometry: **a.** Micro (detailed porous) model, **b.** Macro (homogenized equivalent micropolar) model.

$$\begin{bmatrix} \sigma_{11} \\ \sigma_{22} \\ \sigma_{12} \\ \sigma_{21} \\ \mu_1 \\ \mu_2 \end{bmatrix} = \begin{bmatrix} A_{1111} & A_{1122} & 0 & 0 & 0 & 0 \\ A_{1122} & A_{1111} & 0 & 0 & 0 & 0 \\ 0 & 0 & A_{1212} & A_{1221} & 0 & 0 \\ 0 & 0 & A_{1221} & A_{1212} & 0 & 0 \\ 0 & 0 & 0 & 0 & D_{11} & 0 \\ 0 & 0 & 0 & 0 & 0 & D_{11} \end{bmatrix} \begin{Bmatrix} \varepsilon_{11} \\ \varepsilon_{22} \\ \varepsilon_{12} \\ \varepsilon_{21} \\ \kappa_1 \\ \kappa_2 \end{Bmatrix} \tag{8}$$

Therefore, the stiffness matrix in the current work contains five independent micropolar material parameters. These five parameters are A_{1111}, A_{1122}, A_{1212}, A_{1221}, D_{11}.

It is worth mentioning that in case of an isotropic 2D micropolar model, the number of independent material parameters will decrease to four [26,63,64].

Further, we adopt a different description of the micropolar shear deformation components to directly recognize the first three components of strain as the in-plane Cauchy ones (ε_{11}, ε_{22}, ε_{12}^{SYM}). Thus, the micropolar strain ε will be expressed as:

$$\varepsilon = \left\{ \varepsilon_{11} \quad \varepsilon_{22} \quad \varepsilon_{12}^{SYM} \quad \theta \quad \kappa_1 \quad \kappa_2 \right\}^T \tag{9}$$

where $\varepsilon_{12}^{SYM} = \varepsilon_{12} + \varepsilon_{21}$ is the symmetric shear strain component and $\theta = \varepsilon_{12} - \varepsilon_{21} = 2(\omega - \phi)$ is antisymmetric shear strain component (or rotational deformation, representing two times the difference between the rigid rotation ω and the microrotation field ϕ) where:

$$\omega = \frac{1}{2}\left(\frac{\partial v}{\partial x} - \frac{\partial u}{\partial y}\right) \tag{10}$$

In the case of the couple stress theory and the Cauchy theory, the shear strain is symmetric and θ is equal to zero so that the classical kinematic relations are restored [65].

The work conjugates of these two shear strain measurements, can be defined as:

$$\begin{aligned} \sigma_{12}^{SYM} &= \frac{1}{2}(\sigma_{12} + \sigma_{21}) \\ \sigma_{12}^{ASM} &= \frac{1}{2}(\sigma_{12} - \sigma_{21}) \end{aligned} \tag{11}$$

Where σ_{12}^{SYM} and σ_{12}^{ASM} are symmetric and antisymmetric components of the shear stress.

Finally, we can rewrite Eq. (8) in terms of ε_{12}^{SYM} and θ:

$$\begin{bmatrix} \sigma_{11} \\ \sigma_{22} \\ \sigma_{12}^{SYM} \\ \sigma_{12}^{ASM} \\ \mu_1 \\ \mu_2 \end{bmatrix} = \begin{bmatrix} A_{1111} & A_{1122} & 0 & 0 & 0 & 0 \\ A_{1122} & A_{1111} & 0 & 0 & 0 & 0 \\ 0 & 0 & \frac{A_{1212}+A_{1221}}{2} & 0 & 0 & 0 \\ 0 & 0 & 0 & \frac{A_{1212}-A_{1221}}{2} & 0 & 0 \\ 0 & 0 & 0 & 0 & D_{11} & 0 \\ 0 & 0 & 0 & 0 & 0 & D_{11} \end{bmatrix} \begin{Bmatrix} \varepsilon_{11} \\ \varepsilon_{22} \\ \varepsilon_{12}^{SYM} \\ \theta \\ \kappa_1 \\ \kappa_2 \end{Bmatrix} \tag{12}$$

Since micropolar and Cauchy continua use different degrees of freedom, a kinematic map is required to link the two levels of description. Here, we followed the mapping proposed by Forest and Sab [29] for a square representative volume element (RVE).

The RVE of the porous micromodel and associated u^*, v^* displacement field are shown in Fig. 5**a**.

To replace a heterogeneous material by an equivalent micropolar medium, the local displacement field u^*, v^* in the micro model can be written in terms of the macroscopic displacements u, v, and micro-rotation ϕ as follows (Fig. 5b):

$$\begin{aligned} u^*(x,y) &= u(X,Y) - \phi(X,Y)(y-Y) \\ v^*(x,y) &= v(X,Y) + \phi(X,Y)(x-X) \end{aligned} \tag{13}$$

where (X, Y) are the coordinates of the centre of the RVE (Fig. 5). The best fit of u^*, v^* to the RVE real displacement field u^{real} and v^{real} can be achieved by the least-square minimization of the error over the surface:

$$\begin{aligned} \Delta &= \int_A \left| {u^{real}}_i(x_j) - u_i^*(x_j) \right|^2 dA \\ &= \int_{x=X-L/2}^{x=X+L/2} \int_{y=Y-L/2}^{y=Y+L/2} \left| {u^{real}}_i(x_j) - u_i(X_j) + e_{imn}\phi_m(X_j)(x_n - X_n) \right|^2 dxdy \end{aligned} \tag{14}$$

Which requires:

$$\frac{\partial \Delta}{\partial u} = 0 \qquad \frac{\partial \Delta}{\partial \phi} = 0 \tag{15}$$

By imposing the above conditions, the following relations between the macroscopic micropolar and the microscopic Cauchy displacement fields are derived [66]:

$$\begin{aligned} u &= \frac{1}{A}\int_A u^* dA \\ v &= \frac{1}{A}\int_A v^* dA \\ \phi &= \frac{6}{L^2}\frac{1}{A}\int_A [v^*(x-X) - u^*(y-Y)] dA \end{aligned} \tag{16}$$

As can be seen in Eq. (16), the macroscopic rotational degree of freedom, ϕ, is an average rotation calculated using microscopic translation degrees of freedom, u^* and v^* on the RVE.

Further, a third-order polynomial expression is considered for the displacement field (u^*, v^*) and substituted in Eq. (16). As pointed out in [67], the assumption of polynomial form for the displacement field is an important localisation step which has been adopted commonly in the framework of higher-order homogenisation [68–71].

Then, by using the kinematic relations of Eq. (2) and imposing the invariance conditions described in [29] and [66], the following kinematic map is derived:

$$\begin{aligned} u^* &= \varepsilon_{11}x + \varepsilon_{12}^{SYM}y - \frac{\kappa_2}{2}y^2 - \kappa_1 xy - \frac{10}{L^2}\theta\left(y^3 - 3yx^2\right) \\ v^* &= \varepsilon_{12}^{SYM}x + \varepsilon_{22}y + \frac{\kappa_1}{2}x^2 - \kappa_2 xy + \frac{10}{L^2}\theta\left(x^3 - 3xy^2\right) \end{aligned} \tag{17}$$

Eq. (17) expresses the microscopic displacement field within the RVE as a function of the macroscopic strain measures at the material point on the macro-level [72].

2.4. Identification of micropolar material parameters

After determination of the kinematic map, to find the micropolar material parameters in Eq. (8), first we calculate the response of the porous plate subjected to various loadings. In each case, the corresponding micropolar material parameters are found so that the equivalent material stores the same strain energy density [18,72] when subjected to the identical loading, i.e.:

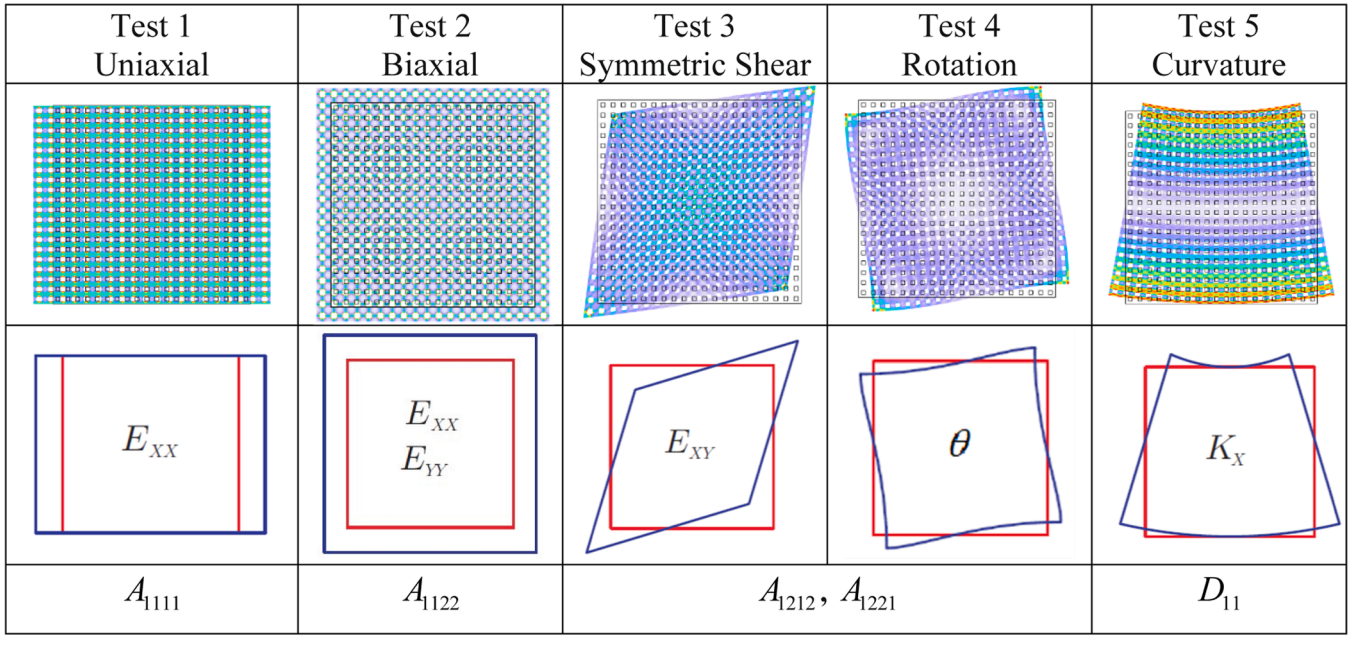

Fig. 6. Designed FEM tests for finding micropolar material parameters.

$$U_{FEM} = U_{Micropolar} \tag{18}$$

Where $U_{Micropolar}$ is the strain energy density of the equivalent micropolar continuum calculated using the following relation:

$$\begin{aligned} U_{Micropolar} &= \frac{1}{2}\left[\varepsilon_{11}\sigma_{11} + \varepsilon_{22}\sigma_{22} + \varepsilon_{12}^{SYM}\sigma_{12}^{SYM} + \theta\sigma_{12}^{ASM} + \kappa_1\mu_1 + \kappa_2\mu_2\right] \\ &= \frac{1}{2}[\varepsilon_{11}(A_{1111}\varepsilon_{11} + A_{1122}\varepsilon_{22}) + \varepsilon_{22}(A_{1122}\varepsilon_{11} + A_{1111}\varepsilon_{22}) + \\ &\quad \varepsilon_{12}^{SYM}\left(\frac{A_{1212} + A_{1221}}{2}\varepsilon_{12}^{SYM}\right) + \theta\left(\frac{A_{1212} - A_{1221}}{2}\theta\right) \quad + \\ &\quad \kappa_1(D_{11}\kappa_1) + \kappa_2(D_{11}\kappa_2)] \end{aligned} \tag{19}$$

And $U_{FEM}$is the strain energy density of the porous plate calculated using the finite element method:

$$U_{FEM} = \frac{1}{2}\int_{RVE} \sigma_{ij}^{p}\varepsilon_{ij}^{p} dV \tag{20}$$

Where σ_{ij}^{p} and ε_{ij}^{p} are stress and strain in the porous structure.

To evaluate the components of the micropolar stiffness tensor ($A_{1111}, A_{1122}, A_{1212}, A_{1221}, D_{11}$), different boundary conditions (tests) are designed to represent uniaxial, biaxial, symmetric shear, bending and rotational deformations. The applied tests and the corresponding material parameters obtained from each test are described in Fig. 6.

The boundary conditions to create each test, are obtained using the micro-filed descriptions of u^*, v^* in terms of macro-field strain measures presented in kinematic map, i.e., Eq. (14).

2.4.1. Test 1: uniaxial extension test to find A_{1111}

A uniform strain $\varepsilon_{11} = 1$ is applied on the porous plate so the boundary conditions can be described as follows:

$$\begin{aligned} u^* &= x \\ v^* &= 0 \end{aligned} \tag{21}$$

And the equivalence of the elastic strain energy density in Eq. (16) will be:

$$\frac{1}{2}[\varepsilon_{11}(A_{1111}\varepsilon_{11})] = U_{FEM,1} \tag{22}$$

which gives:

$$A_{1111} = 2U_{FEM,1} \tag{23}$$

2.4.2. Test 2: biaxial extension test to find A_{1122}

To apply bi-axial uniform strains $\varepsilon_{11} = \varepsilon_{22} = 1$ on the porous plate, the corresponding boundary conditions should be:

$$\begin{aligned} u^* &= x \\ v^* &= y \end{aligned} \tag{24}$$

And the equivalence of the elastic strain energy density leads to:

$$\frac{1}{2}[\varepsilon_{11}(A_{1111}\varepsilon_{11} + A_{1122}\varepsilon_{22}) + \varepsilon_{22}(A_{1122}\varepsilon_{11} + A_{1111}\varepsilon_{22})] = U_{FEM,2} \tag{25}$$

giving:

$$A_{1122} = U_{FEM,2} - A_{1111} \tag{26}$$

2.4.3. Test 3: symmetric shear deformation test to find $A_{1212} + A_{1221}$

To apply uniform shear strain $\varepsilon_{12}^{SYM} = 1$ on the equivalent micropolar media, the corresponding boundary conditions for the micromodel (porous plate) should be:

$$\begin{aligned} u^* &= y \\ v^* &= x \end{aligned} \tag{27}$$

Which results in the following elastic strain energy equivalence:

$$\frac{1}{2}\left[\varepsilon_{12}^{SYM}\left(\frac{A_{1212} + A_{1221}}{2}\varepsilon_{12}^{SYM}\right)\right] = U_{FEM,3} \tag{28}$$

2.4.4. Test 4: rotational deformation test to find $A_{1212} - A_{1221}$

To apply uniform rotational deformation $\theta = 1$ on the equivalent micropolar media, the following should be the corresponding boundary conditions for the porous plate:

$$\begin{aligned} u^* &= +\frac{10}{L^2}\left(y^3 - 3yx^2\right) \\ v^* &= -\frac{10}{L^2}\left(x^3 - 3xy^2\right) \end{aligned} \tag{29}$$

and the equivalence of strain energy density gives:

$$\frac{1}{2}\left[\theta\left(\frac{A_{1212} - A_{1221}}{2}\theta\right)\right] = U_{FEM,4} \tag{30}$$

Using the results of the rotational and symmetric shear tests (Eqs. (28) and (30)) together, A_{1212} and A_{1221} can be found individually:

$$\begin{aligned} A_{1212} &= 2\left(U_{FEM,3} + U_{FEM,4}\right) \\ A_{1221} &= 2\left(U_{FEM,3} - U_{FEM,4}\right) \end{aligned} \tag{31}$$

2.4.5. Test 5: uniform bending test to find D_{11}

Finally, for the uniform curvature $\kappa_1 = 1$on the equivalent micropolar media, the corresponding boundary conditions will be applied on the porous plate:

$$\begin{aligned} u^* &= -\,xy \\ v^* &= x^2/2 \end{aligned} \tag{32}$$

Resulting in the following the elastic strain energy equivalence:

$$\frac{1}{2}\left[\kappa_1\left(D_{11}\kappa_1\right)\right] = U_{FEM,5} \tag{33}$$

which leads:

$$D_{11} = 2U_{FEM,5} \tag{34}$$

The boundary conditions applied in the FEM tests are according to the displacement field specified in Sections 2.4.1 to 2.4.5. These boundary conditions are consistent with the relations of the periodic boundary condition detailed in [71] and therefore, intrinsically implies periodicity.

3. Finite element implementation

The finite element method (FEM), implemented in COMSOL Multiphysics, is used to discretise the problem at both the macro and microlevels. The detailed porous structure was meshed using the first order (linear) triangular elements. The thickness of the GBR plate is considered as 1/100 of the length of the plate and therefore 2D plane stress formulation for linear elastic media was adopted. The convergence of the mesh size was studied based on the values extracted for strain energies (U_{FEM}). The applied boundary conditions are the ones that are described in Sections 2.4.1. to 2.4.5. To implement the micropolar continuum numerically, we used the capability of COMSOL Multiphysics to apply the weak form to partial differential equations (PDE). The reason for this is that the FEM for the micropolar theory or other non-classical continua is not yet available in commercial FE codes. By using PDE modelling in COMSOL instead of traditional FE modelling, no user subroutines are required and various complex geometries, boundary conditions, and loadings can be applied in a user-friendly graphical interface. For the homogenous equivalent models, structured quadrilateral elements, and first-order (linear) discretization (for both displacements and micro-rotation) were applied. The formulation of the elements is described by the constitutive equations explained in 2.3.

To develop the weak form [14], we start from the balance equations in Eq. (2) and multiply each of the two equations by the test functions corresponding to the unknowns u_i and ϕ, denoted here as v_u and v_ϕ, and integrate over the entire computational domain D and by using the divergence theorem and considering B as the surface boundary, the weak form PDE can be defined:

$$-\int_D \sigma_{ij} v_{ui,j} + \int_B \sigma_{ij} v_{ui} n_j + \int_D p_i v_{ui} = 0 \tag{35}$$

$$-\int_D \mu_{kj} v_{\phi,j} + \int_B \mu_{kj} v_{uk} n_j - \int_D e_{ijk}\sigma_{ij} v_\phi + \int_D q_k v_\phi = 0 \tag{36}$$

Table 1
Material properties for the simulations [60].

Material Properties	Unit	Titanium alloy (Ti6Al4V)
Young's Modulus	GPa	114
Poisson Ratio	–	0.3
Density	kg/m^3	4500

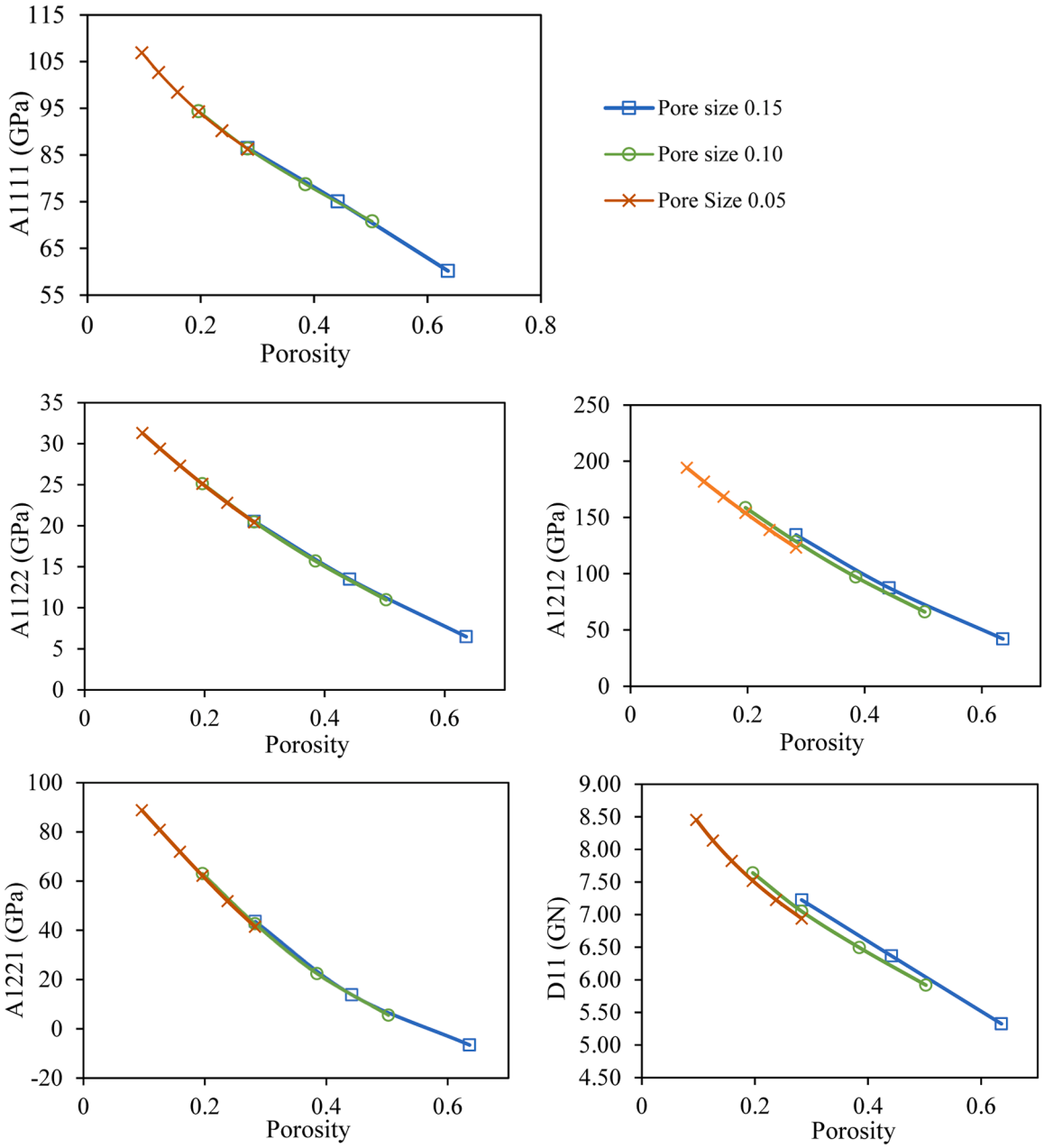

Fig. 7. Equivalent material parameters from micropolar homogenised model for GBR mesh with circular pores (each dataset shows results for a specific pore size and various number of pores).

The convergence of the implemented mesh was studied for each loading case where the study of the equivalent micropolar model showed that the minimum mesh size of 0.05 L was the proper value for achieving discretization independency. The maximum difference of the results for the magnitude of displacements was less than 0.1 % for the mesh size of 0.02 compared to the mesh size of 0.05 L.

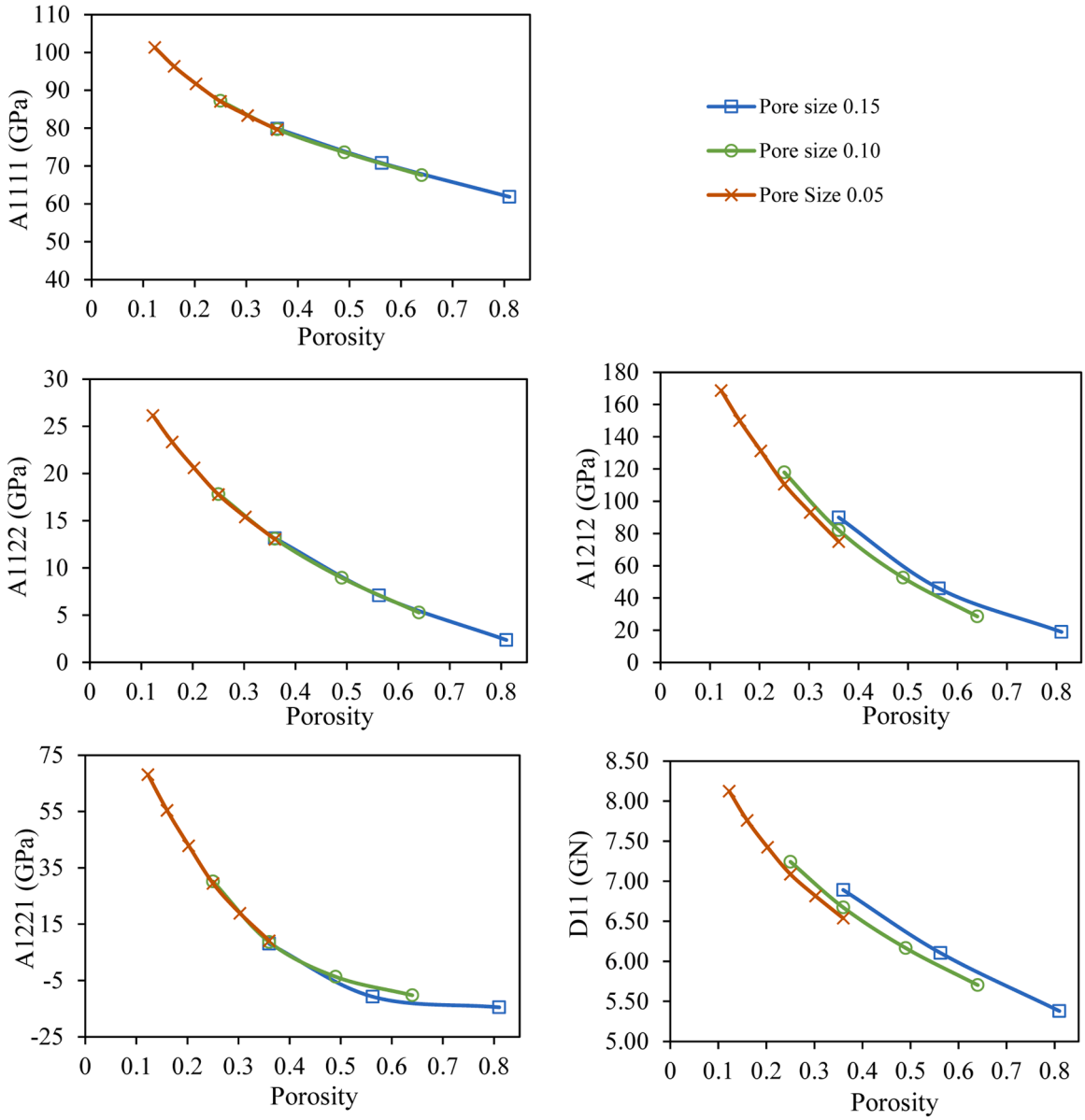

Fig. 8. Equivalent material parameters from micropolar homogenised model for GBR mesh with square pores (each dataset shows results for a specific pore size and various number of pores).

The developed FEM micropolar model was tested with the available benchmarks from the literature to assess the accuracy and flexibility of the code. The results of the three patch tests introduced in [73] were consistent with the analytical solutions as benchmark values. The independence of the results from linear and bilinear discretization as well as from structured rectangular and triangular meshes (fine and coarse meshes) was also investigated. As a second check, the numerical study of a micropolar linear elastic plate with a circular hole under uniform tensile stress showed a good agreement with the stress concentration factors from [64]. Also, the displacement fields shown in [17] for an orthotropic micropolar FEM model matched the findings of this study. Such benchmarks are not reported here for the sake of conciseness and also because they are out of the scope of the present research work.

The developed FEM micropolar model has some limitations and assumptions. The accuracy of the results may be influenced by the quality of the mesh and can be remedied through mesh convergence study. Material properties are assumed to be constant and homogenous throughout the structure. The accuracy of the results may be sensitive to the prescribed boundary conditions, which are simplified to be applicable within the weak form PDE framework. The weak form involves simplifying the strong form of the equations and 2D plane stress formulation is an approximation of the real 3D problem. Adjusting solver settings involves trade-offs between accuracy and computational cost.

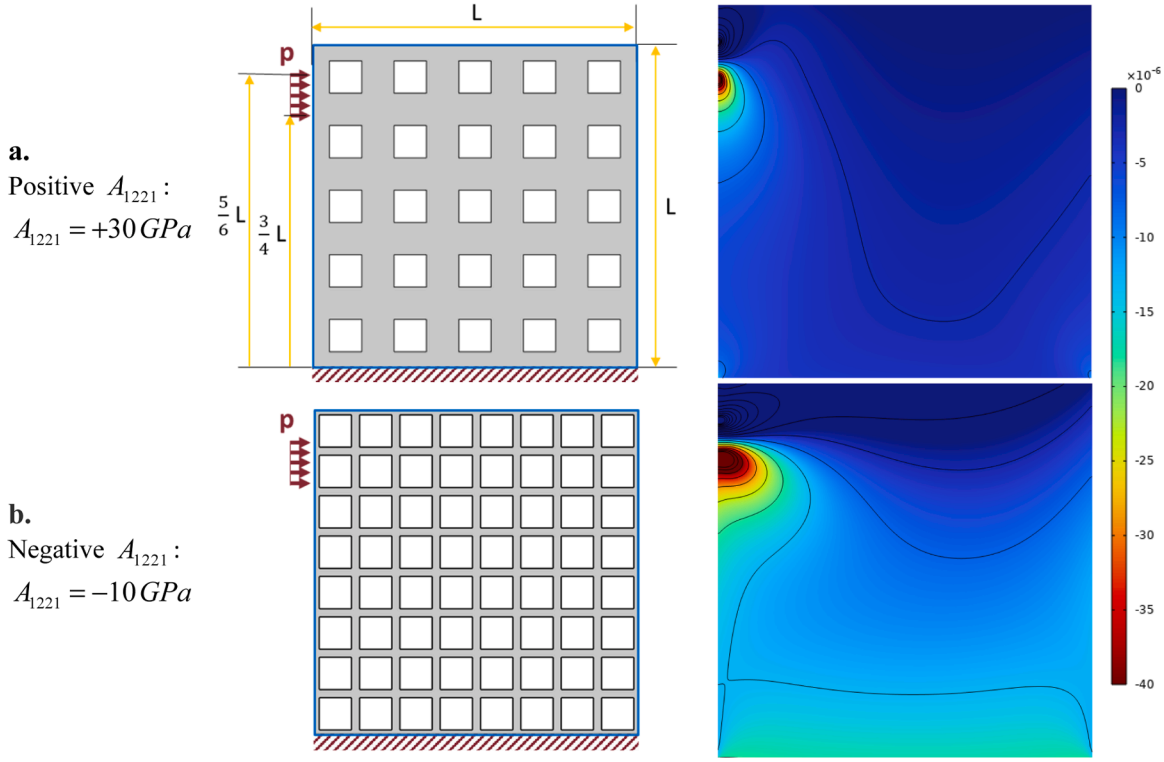

Fig. 9. The geometry, applied loading and boundary conditions applied on the equivalent micropolar model to evaluate the effect of A_{1221}on the local rotation $2\theta = (\omega - \phi)$ **a.** case 1: square-shaped pore with positive A_{1221}, $l_p = 0.1L$ and $N_p = 5$ **b.** case 2: square-shaped pore with negative A_{1221}, $l_p = 0.1L$ and $N_p = 8$.

4. Numerical results and discussion

In the following section, numerical results regarding parametric studies on GBR meshes with circular and rectangular pores are presented and discussed.

The material properties assumed for the porous structure, is the common titanium alloy available as GBR mesh sheets in the market. The properties of this alloy are listed in the Table 1.

4.1. Circular pores

Fig. 7 presents the equivalent micropolar material parameters for a GBR mesh with circular pores. Each dataset shows the results for a specific pore size and various number of pores. For a better insight, the material parameters are shown with respect to the porosity, which is the ratio of the pores' surface area to the total surface area and is calculated using the following relation:

$$Porosity = \frac{(N_{pore})^2 \cdot \frac{\pi}{4} (L_{pore})^2}{L^2} \tag{37}$$

4.2. Square pores

To evaluate the effect of pore geometry, Fig. 8 presents the equivalent micropolar material parameters for meshes with rectangular pores (Fig. 3). The pattern is parametrized using the rectangular pore side as the pore size, L_{pore}, and the number of pores, N_{pore}. The porosity is calculated by the following equation:

$$Porosity = \frac{(N_{pore})^2 \cdot (L_{pore})^2}{L^2} \tag{38}$$

4.3. Size effect in the micropolar homogenised model

By studying the porosity trends in Figs. 7 and 8, one can recognize that A_{1111} and A_{1122} depend only on the value of porosity and pore size has no significant effect. This means that the variation of these two material properties can be described by porosity as a single

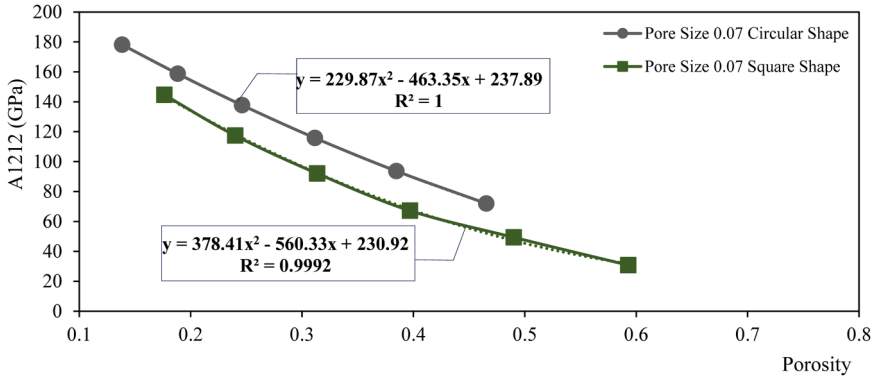

Fig. 10. The comparison of the A_{1212} for circular and square pore shapes, as well as the fitted second order polynomials for each data set. (The curve-fitting value R^2 =1 denotes a perfect fit.).

variable. This can also be described by classical theories [18] according to which the stiffness of porous materials decreases with increasing porosity regardless of the characteristic length of the pores (see for instance, [74–77]). As a matter of fact, the A_{1111} and A_{1122} correspond to the same quantities of the constitutive matrix for an equivalent Cauchy material.

However, for the other three material parameters corresponding to the micropolar theory, the pore size affects the material parameters even if the total porosity is the same, which means that it is no longer possible to describe the variation of the material parameters by a single variable such as porosity. The difference is more prominent as the pore size increases and the internal characteristic length becomes comparable to the overall dimension of the plate. This observation is consistent with the inherent ability of micropolar theory to account for the internal structure and the size effects in the material. Some evidence from literature (ex. [75]) also has shown this observation.

4.4. Negative A1221 for higher porosities

According to Figs. 7 and 8, for higher porosities, values of A_{1221} for both circular and square pores become negative, which means that shear loading in one direction, counter clockwise for instance, ($\sigma_{12} Counter-clockwise$, $\sigma_{21}=0$, $\varepsilon_{12} Counter-clockwise$), results in counter clockwise ε_{21}.The behaviour toward shear loading can be analogous to what auxetic material (negative Poisson's ratio) [78] exhibits with respect to axial loading. It can be concluded that the deformation mechanism changes for higher porosities (beginning at 50–60 percent). At lower porosities, the deformation is controlled by the stiffness of the base material, but as the porosity increases and the volume of the material decreases, the pores take control of the deformation.

According to Eq. (12), $\frac{(A_{1212}-A_{1221})}{2}$ is the coefficient related to the antisymmetric shear strain component, θ, and $\frac{(A_{1212}+A_{1221})}{2}$ is the coefficient related to the symmetric shear strain, ε_{12}^{SYM} . When the A_{1221} get negative, the value of $\frac{(A_{1212}-A_{1221})}{2}$ is still positive in rotational test while it is larger than $\frac{(A_{1212}+A_{1221})}{2}$ from the shear test. Therefore, the sign of θ is not changed in rotation test and is always positive.

However, when A_{1221} gets negative, the rotation mode (Asymmetric Shear) becomes dominant and θ is higher compared to similar loading and boundary condition for a porous structure with positive A_{1221}. For a better demonstration, Fig. 9 shows the local rotation value ($2\theta=(\omega-\phi)$) in a porous structure under shear loading for two cases of positive and negative A_{1221}.

As can be seen in Fig. 9, where A_{1221} is negative, the value and distribution of the local rotation is much more dominant, therefore micropolar effect is much more evident with respect to a Cauchy model that considers zero relative rotation.

4.5. Effect of pore shape

In the current work, two circular and square pore shapes with regular patterns are presented to point out the influence of pore geometry/pattern on the mechanical parameters of GBR meshes. Through the proposed procedure, a variety of different geometries and patterns (see Fig. 2b) can be considered and studied.

By comparing the results of the circular and rectangular pore shapes (Figs. 7 and 8), it can be deduced that by choosing square shape pores leads to a wider range of possible porosities as they can provide a more compact arrangement. This can be helpful in meeting biomedical porosity requirements while providing the desired stiffness.

Despite the difference between the values of both pore shapes, the overall trend of the stiffness parameters can be well approximated by a parabolic curve with respect to the porosity. This observation is well consistent with the results for stiffness of closed-cell porous materials with constant wall thickness (see p. 196 of [15]). As an example, the fitted parabolic curves for the coefficient of A_{1212} for both pore shapes are presented in Fig. 10 for the pore size of 0.07.

Table 2
Micropolar material characteristics for compact bone [50,51,79,80].

Parameter	Symbol	Unit	Value
Shear Modulus	G	MPa	4000
Poisson's Ratio	ν	–	0.25
Coupling Number	N	–	0.5 ∼ 0.9
Characteristic Length (Bending)	l_b	m	0.00045

Table 3
Micropolar stiffness matrix components for bone extracted from experimental data (Table 2).

Parameter	Unit	Value
A_{1111}	GPa	12.00 ∼ 43.43
A_{1122}	GPa	4.00
A_{1212}	GPa	21.10 ∼ 36.77
A_{1221}	GPa	−13.05 ∼ 2.67
D_{11}	kN	3.24

4.6. GBR mesh application

An experimental estimate of the micropolar parameters of compact bone is shown in Table 2. These values are given in [79,80] based on the experimental tests in [51,54], where the material parameters for an isotropic micropolar model are obtained using the observed size effects in quasi-static bending of sample compact bone.

For an ortho-tetragonal elastic micropolar material model (see [44,63]), considering the material parameters introduced in Eq. (8) and those reported in Table 2, the coefficients of stiffness matrix, can be found as presented in Table 3 for the bone when considered as a micropolar material. These values are shown as highlighted yellow regions in Fig. 11.

Now the comprehensive data provided in Figs. 7, 8 allows us to find a configuration with the material parameters close to those reported in Table 3. For instance, as it can be observed in Fig. 7, the material parameters for the circular pores are beyond the required values. However, in case of rectangular pore patterns (Fig. 8) with a size of 0.13 ∼ 0.15 and porosity about 0.7, a good agreement for A_{1122}, A_{1212}, A_{1221} can be achieved (see Fig. 11 in which the highlighted yellow area indicates the material parameter which corresponds to the compact bone).

From a mechanical point of view, to avoid stress shielding, it is important that bone scaffolds mimic the mechanical environment of the host bone. Therefore, according to the experimental data in Table 3 for the cortical bone and the parametric studies in Sections 4.1 and 4.2, as a finding of the present study, we propose to use titanium membrane with rectangular pore patterns with a size of $0.13\,L \sim 0.15\,L$ and porosity about 70 %. This pattern can lead to the micropolar parameters that are close to that of the compact bone measured experimentally.

Regarding the morphology of the patterns, according to the experiments Van Bael et al. [81], the presence of corners in the pores can increase the cell growth [82], therefore we suggest that the choice of rectangular patterns is favourable over the circular ones.

The choice of $0.13\,L \sim 0.15\,L$ (where L as the overall length of dental GBR mesh is around one centimetre) for the pore size allows for enough permeability for the nutrients. The value of 1.3 mm to 1.5 mm for the pore size is in favour with the experimental observation of Gutta et al. [8] where they reported that macro-pores of more than 1 mm in the titanium membrane promote better bone regeneration [3].

More studies on other materials (for example, bio-degradable materials such as PLA [83], PLA composites [84]) and other pore shapes and patterns can be helpful to find agreements for all the parameters. It should be noted that the material parameters presented in Table 3 are derived based on the experiments on samples of compact bone from the femur bone [51], and further experimental testing for the mandible bone can lead to finding much more reliable material parameters. In addition, real bone has the structure of a functionally graded material (FGM), and this could be considered for designing bimodal [85] or functionally graded [86–89] porous structures of GBR meshes.

4.6.1. Cauchy homogenised model

To evaluate the effectiveness of the micropolar theory in homogenising the porous structure and its superiority to the homogenised Cauchy model, the analogous approach is followed in the framework of Cauchy theory.

The stress-strain relation for the two-dimensional ortho-tetragonal material can be written in Voigt notation as:

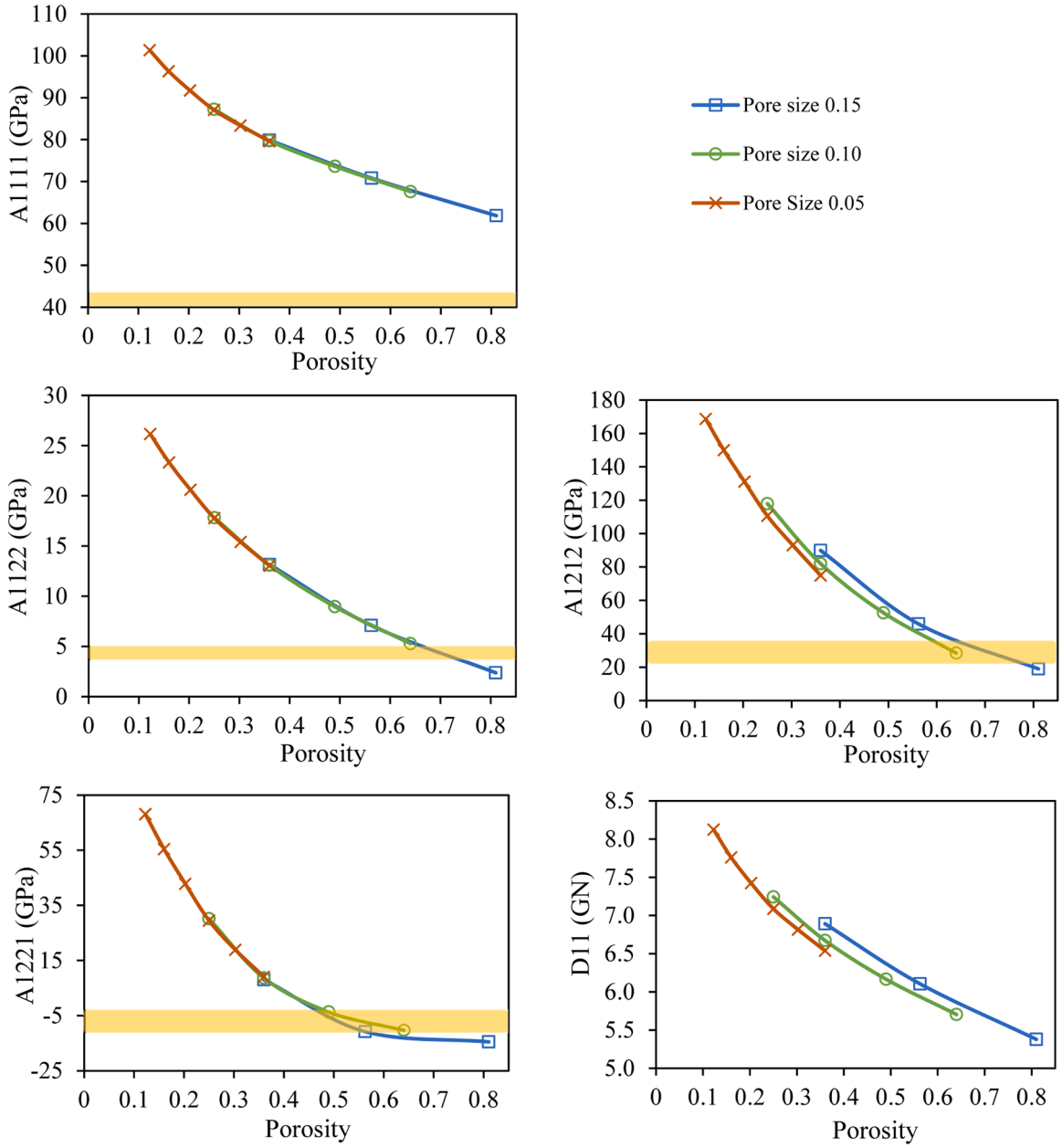

Fig. 11. Equivalent material parameters from micropolar homogenized model. The yellow area indicates the compact bone equivalent parameters.

$$\begin{Bmatrix} \sigma_{11} \\ \sigma_{22} \\ \sigma_{12} \end{Bmatrix} = \begin{bmatrix} C_{1111} & C_{1122} & 0 \\ & C_{1111} & 0 \\ sym. & & C_{1212} \end{bmatrix} \begin{Bmatrix} \varepsilon_{11} \\ \varepsilon_{22} \\ \gamma_{12} \end{Bmatrix} \tag{39}$$

For which the Voigt stiffness matrix has three independent material parameters. Therefore, according to Eq. (39), the Cauchy model for the two-dimensional ortho-tetragonal material requires three independent material parameters, while according to Eq. (8) for a 2D ortho-tetragonal micropolar model, the number of independent constitutive parameters is five.

An analogous procedure to the first three tests in Section 2.4 is followed to find equivalent Cauchy material parameters, which we avoid repeating for the sake of brevity. The three tests—uniaxial, biaxial, and shear—are carried out for the purpose of evaluating the

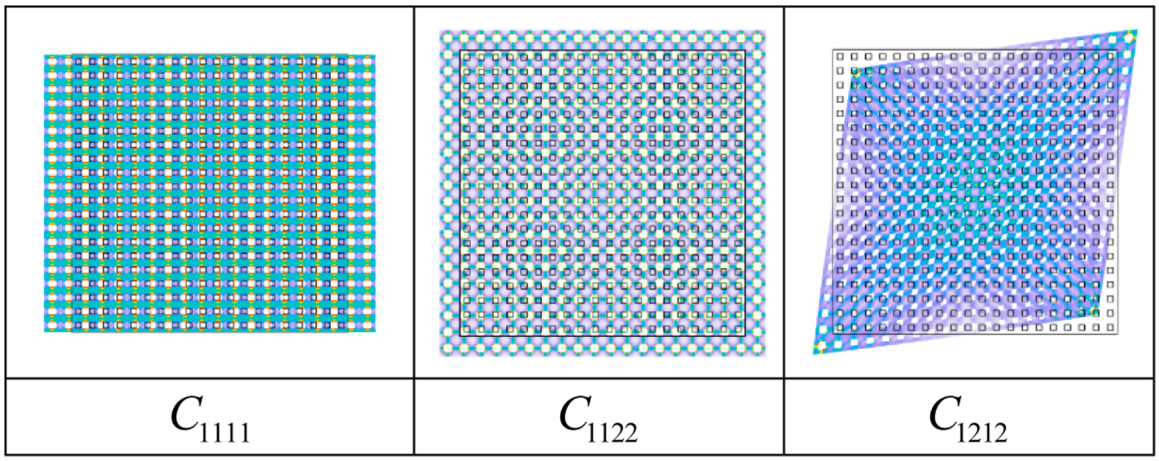

Fig. 12. Designed FEM tests for finding Cauchy material parameters.

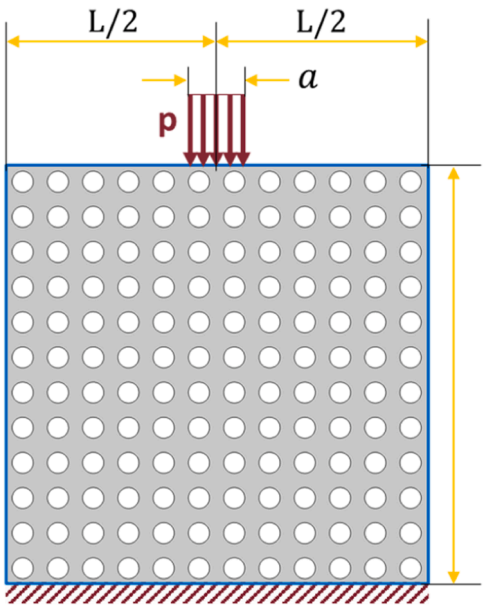

Fig. 13. The geometry, loading and boundary conditions to evaluate the homogenised micropolar model.

components of Cauchy stiffness matrix (C_{1111}, C_{1122}, C_{1212}). These tests are presented in Fig. 12.

4.6.2. The competence of micropolar theory to the Cauchy theory in describing GBR meshes

There are two main reasons for using micropolar theory instead of Cauchy theory in the modelling and describing the physical response of porous GBR meshes: firstly, the presence of internal structure in the porous meshes can be better described with micropolar theory as it is able to preserve the memory of the material's internal structure through internal scale parameters, ϕ. Particularly the difference between micropolar and Cauchy theories is more dominant when the size of the pores in the material becomes comparable to the size of the overall structure. To highlight this point, the indentation of a vertical load on a porous square plate (Fig. 13) is investigated for both circular and square pores with different pore sizes. The parameters used for the simulations are:

$$p = 10,000 \qquad L = 1 \quad L_{pore} = 0.03L,\ 0.05L,\ 0.07L \quad N_{pore} = 12 \qquad a = L/10.$$

The magnitude of the displacement for the real porous structure, homogenised Cauchy model and the homogenised micropolar

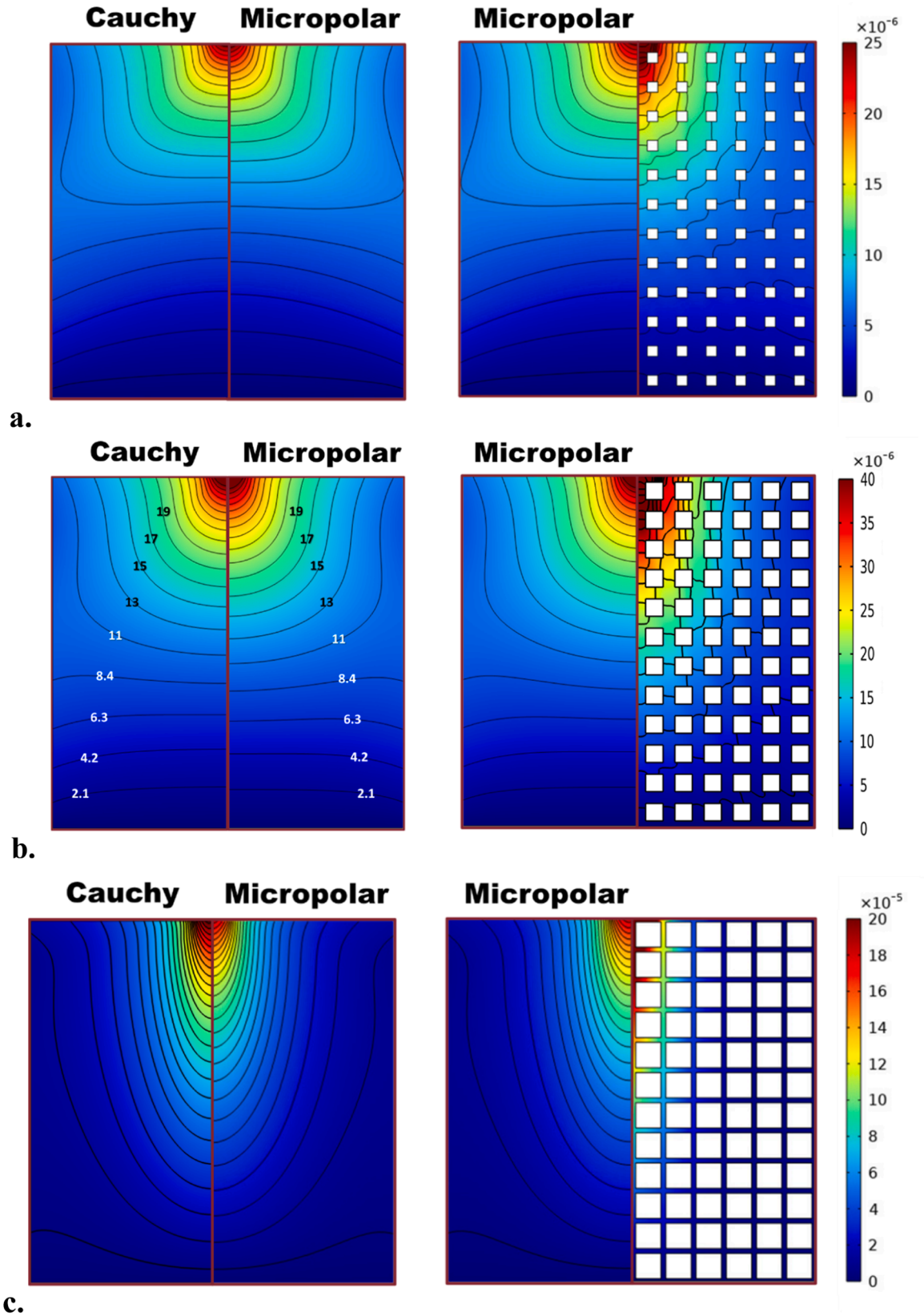

(caption on next page)

Fig. 14. The comparison of the total displacement magnitude for the homogenized micropolar and Cauchy models with the detailed porous structure for square pores ($N_{pore} = 12$) with three different pore sizes; **a.** $L_{pore} = 0.03L$ **b.** $L_{pore} = 0.05L$ and **c.** $L_{pore} = 0.07L$.

model are shown in Figs. 14 and 15. Also, for better comparison, the values of the displacements are labelled on the corresponding contour lines in Fig. 14b. As shown in Figs. 14 and 15, the displacement contour lines predicted by micropolar theory are placed deeper in height compared to the displacement contours predicted by Cauchy theory. Considering that the deeper prediction of micropolar theory is closer to the displacement of the real porous structure, the load penetration reflected in the displacement contours, is better captured by the micropolar theory.

A comparison of Fig. 14a and b also shows that as the pore size increases, the difference between the micropolar and Cauchy predictions increases, indicating the preference for the micropolar theory when the size of the inner structure becomes comparable to the external structure.

Besides, when comparing Figs. 14 and 15, it can be observed that the difference between the two theories is more pronounced for square patterns, which could be because the RVE is less sensitive to local rotation in circular patterns compared to square patterns.

Finally, according to some experimental observations, the micropolar theory provides better predictions of the mechanical response of the bone than the Cauchy theory. Therefore, a bone implant is mechanically more consistent with the adjacent bone if it has the same micropolar constants as experimentally determined for the bone.

4.7. Absolute size dependence of micropolar parameters

In order to study the effect of microstructure absolute size on the determined parameters, in Fig. 16a and b, the variation of C_{1111}(A_{1111} in micropolar), and A_{1212} are plotted with respect to the edge length (L_{UC}) for the square-pore pattern. The number of squares (unit cells) in each direction are varied so that the porosity is kept constant to 42 % for all the RVEs (Fig. 18c).

As seen in Fig. 16, the Cauchy effective modulus remains invariant when the dimension of the unit cell changes. This observation aligns with the characteristic of Cauchy elasticity, which lacks any inherent length scale and therefore the Cauchy parameter remains unaltered for self-similar unit cells with the same porosity [90] while, the micropolar effective moduli exhibit a variation with respect to the length of the unit cell which shows its capability in capturing microstructural feature.

It should be noted that increasing the stiffness of the material when the internal structures become comparable to the external dimension is one the features of heterogenous materials that is conveniently captured through micropolar theory.

On the other hand, surface-related mechanics suggests that the surface properties can affect mechanical response of a material where one of the consequences is the size dependence of effective mechanical properties [90]. For the structures shown in Fig. 16, the ratio of the pores' free surface to the material's volume changes from 58 to 4 and the change in this ratio is well reflected in the obtained micropolar mechanical parameters, whereas, the effect of surface/volume is not accounted for by Cauchy theory as it predicts the same value for all surface to volume ratios.

4.8. Study of the result's affecting parameters

Fig. 17a describes the study of the dependence of the micropolar moduli with respect to the number of the unit cells (UC) in an RVE for the square pore pattern and the pore length of 0.05 L. The curves in Fig. 18b show the change of the obtained micropolar parameters with respect to the number of repetition of UCs. As can be seen, the constitutive parameters that are common in the micropolar and Cauchy theories (A_{1111}, A_{1122}) are almost invariant to the number of the UC, while the parameters related to the micropolar model (A_{1212}, A_{1221}, D_{11}) are dependent especially before 3 repetitions of UCs. This observation is consistent with [69] where the effect of UC on the homogenised micromorphic parameters of a heterogenous periodic composite is studied. In the current work, we chose nine repetitions of UC to ensure a convergence of more than 99.5 %.

In addition, several uncertainties may arise based on the assumptions in the current work: material properties, including their characterisation and the choice of constitutive models, introduce uncertainties that may affect the accuracy of the results. By conducting a sensitivity analysis to assess the effects of variation of elastic properties of the texture material (Young's modulus and Poisson's ratio) on the obtained equivalent micropolar parameters, we observed that the sensitivity to changes in Poisson's ratio is several orders of magnitude higher than that of Young's modulus. However, this uncertainty can be dealt with by considering the limited range of Poisson's ratio ($-1 \sim 0.5$) and the reliable value of 0.3 for the metallic titanium alloy used in this work. (ASME B31.1, [60,91]) The boundary conditions can also lead to uncertainties. In this study, they are enforced by the primary dependent variables (displacements and micro-rotations) to achieve better control.

5. Conclusions

The main purpose of the current work was to demonstrate the effectiveness of the equivalent micropolar model to account for the internal structure in a porous plate without directly modelling the pores. A multi-scale homogenization procedure was presented for

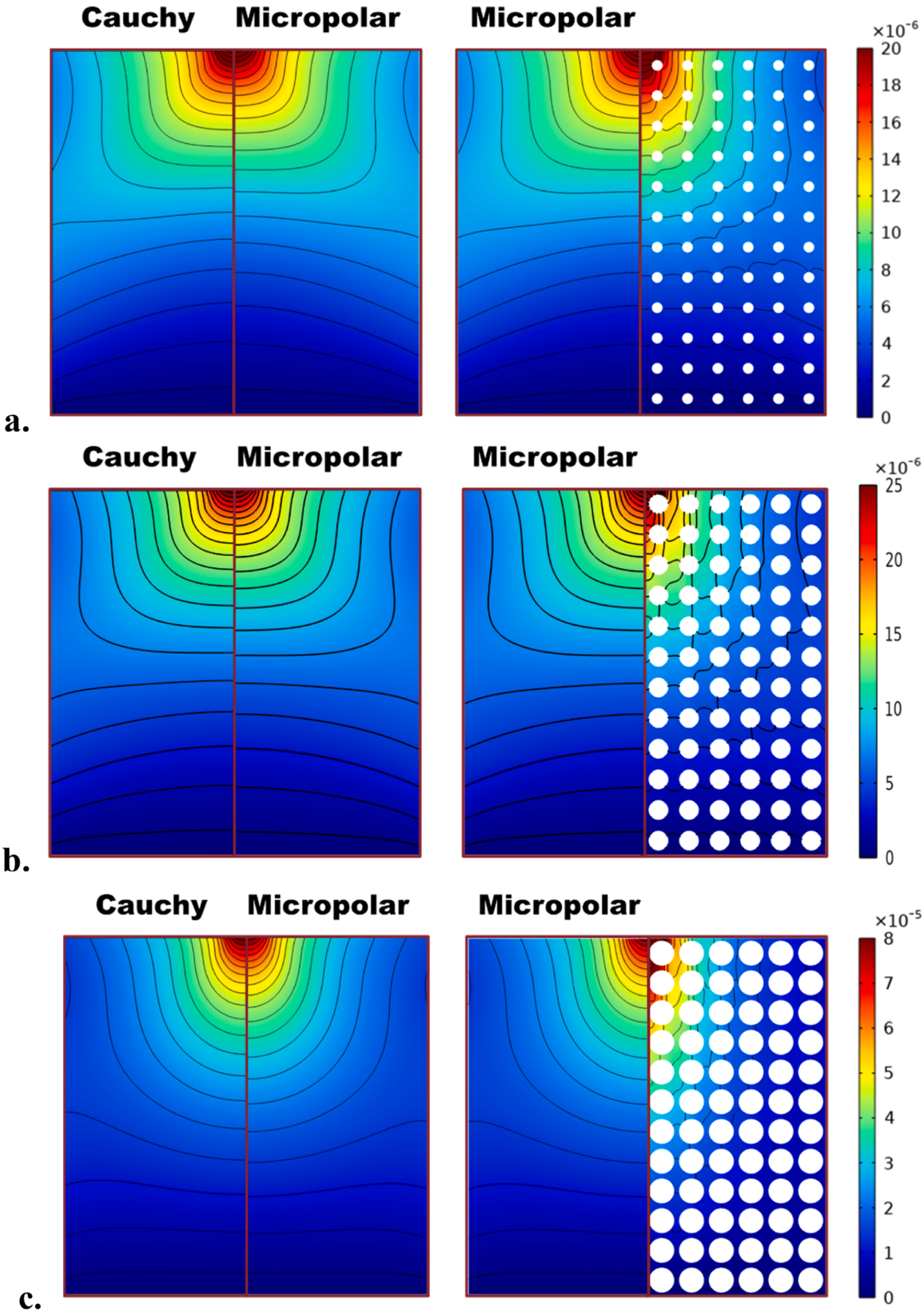

(caption on next page)

Fig. 15. The comparison of the total displacement magnitude for the homogenized micropolar and Cauchy models with the detailed porous structure for circular pores ($N_{pore} = 12$) with three different pore sizes; **a.** $L_{pore} = 0.03L$ **b.** $L_{pore} = 0.05L$ and **c.** $L_{pore} = 0.07L$.

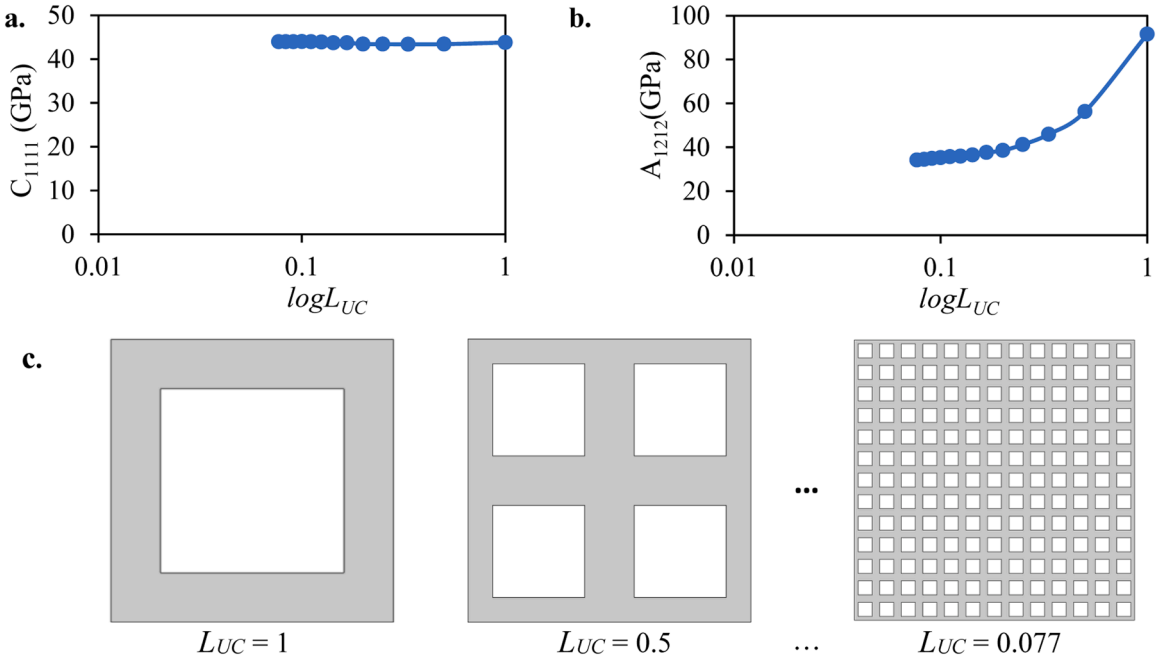

Fig. 16. The study the effect of microstructure absolute size on the determined parameters at the same porosity for the square-shape pores **a.** Variation of C_{1111} with respect to length of the unit cells **b.** Variation of A_{1212} with respect to length of the unit cells **c.** The edge length of the unit cells in the studied RVEs are changed so that the porosity remains constant. (The edge length, L_{UC}, are normalised to the size of the RVE).

two-dimensional porous media, used as GBR mesh in dentistry, based on the adoption of micropolar continuum that can account for microstructural features. The homogenization is based on the equivalence of strain energy of the porous micropolar model under specified boundary conditions. The influence of the porosity parameters, namely pore size, pore density and shape, on the obtained effective mechanical moduli has been analysed.

The main findings can be summarized as listed below:

- The micropolar homogenised model follows the real deformation of the porous structure better than the homogenised Cauchy model, especially near the load application.
- Different material parameters are obtained with the same porosity and different pore size, especially when the pore size becomes comparable to the overall size of the structure. In this case, the variation of elastic moduli cannot be described by the porosity parameter alone. The overall trend of the micropolar moduli can be well approximated by a parabolic curve as a function of porosity. However, this curve also depends on the pore size for higher ratio of pore size to plate size.
- Pore geometries that result in more compact patterns are a better choice for GBR meshes as they can provide a broader range of porosity leading to more flexibility in designing mechanical parameters.
- To avoid stress shielding, it is important that bone scaffolds mimic the mechanical environment of the host bone. As a finding of the present study, we propose to use titanium membrane with rectangular pore patterns with a size of 0.13 $L \sim 0.15$ L and porosity about 70 %. This pattern can lead to the micropolar parameters that are close to that of the compact bone measured experimentally.
- The equivalent micropolar mechanical constants can be used together with the bone parameter data available in the literature or by further experimentation on the mandibular bone samples to find a better design of GBR meshes that have similar mechanical parameters to the underlying bone.
- This micropolar model was found to be effective to account for the internal structure in the porous plate without directly modelling the pores. The data provided here can be used to simulate the performance of porous GBR meshes in operation without incurring in unnecessary computational costs.

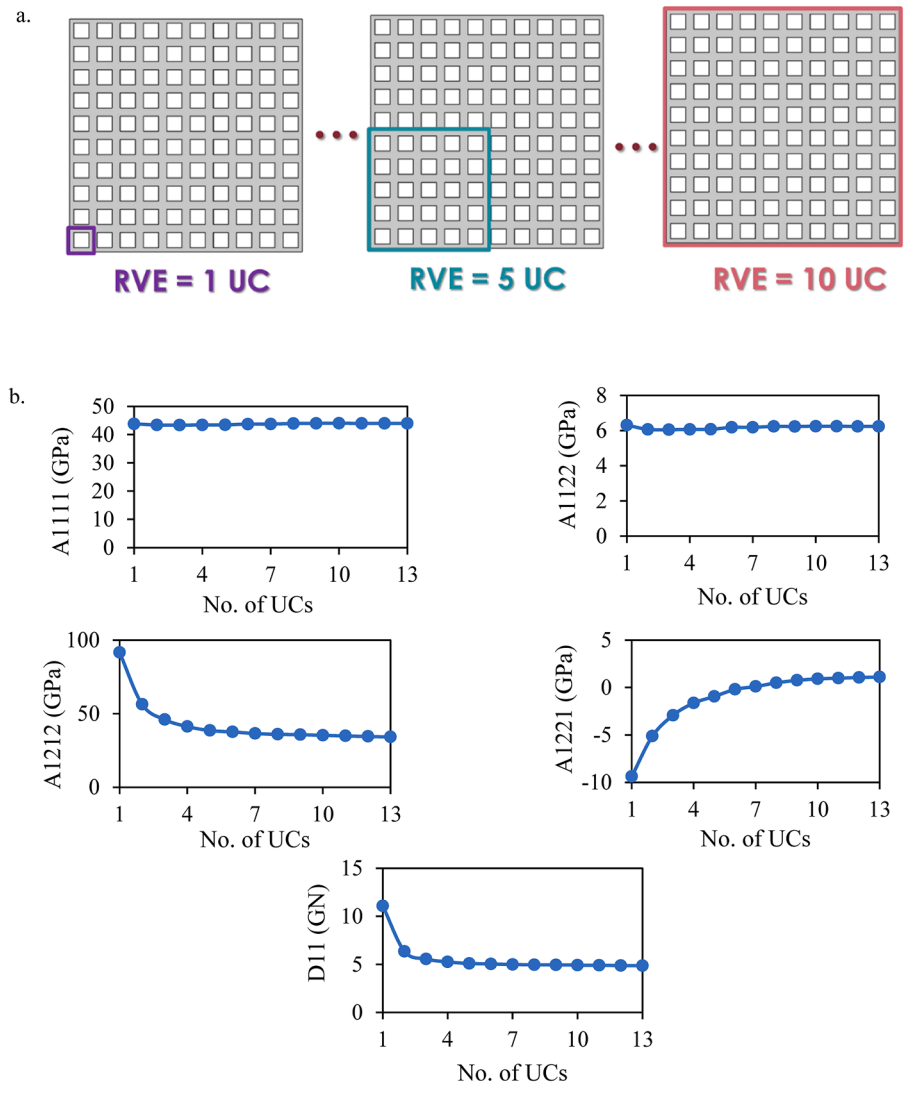

Fig. 17. The study of dependence of the micropolar to number of unit cells in the RVE for the square pore pattern and the pore length of 0.05 L. a. RVEs with different number of repetitions of unit cells b. Variation of the material parameters versus the number of UCs .

Future developments of the current work include the evaluation of other pore patterns and shapes as well as the consideration of functionally graded (FG) patterns [22] to optimize porosity and stiffness requirements with the ability to mimic the bone's characteristics [86]. Another direction to extend the results of the work would be to consider stochastic porous structures [92] and evaluate their mechanical properties using the homogenization method implemented here.

Declaration of competing interest

The authors declare that they have no known competing financial interests or personal relationships that could have appeared to influence the work reported in this paper.

Data availability

Data will be made available on request.

Acknowledgements

This work has been supported by PRIN 2020, project 2020F23HZ7_003 (grant number: J35F22000640001). Ministry of University and Research (MUR).

References

[1] Y.D. Rakhmatia, Y. Ayukawa, A. Furuhashi, K. Koyano, Current barrier membranes: titanium mesh and other membranes for guided bone regeneration in dental applications, J. Prosthodont. Res. 57 (1) (2013) 3–14, https://doi.org/10.1016/j.jpor.2012.12.001. Jan.
[2] Z. Yang, et al., Advances in barrier membranes for guided bone regeneration techniques, Front. Bioeng. Biotechnol. 10 (2022), https://doi.org/10.3389/fbioe.2022.921576. Jun.
[3] I. Elgali, O. Omar, C. Dahlin, P. Thomsen, Guided bone regeneration: materials and biological mechanisms revisited, Eur. J. Oral Sci. 125 (5) (2017) 315–337, https://doi.org/10.1111/eos.12364. Oct. 01,.
[4] A. Scribante, et al., Full-digital customized meshes in guided bone regeneration procedures: a scoping review, Prosthesis 5 (2) (2023) 480–495, https://doi.org/10.3390/prosthesis5020033. MDPIJun. 01,.
[5] T.V. Scantlebury, 1982-1992: a decade of technology development for guided tissue regeneration, J. Periodontol. 64 (1993) 1129–1137, https://doi.org/10.1902/jop.1993.64.11s.1129, no. 11sNov.
[6] A.K. Lundgren, L. Sennerby, D. Lundgren, A. Taylor, J. Gottlow, S. Nyman, Bone augmentation at titanium implants using autologous bone grafts and a bioresorbable barrier. An experimental study in the rabbit tibia, Clin. Oral Implants Res. 8 (2) (1997) 82–89, https://doi.org/10.1034/j.1600-0501.1997.080202.x. Apr.
[7] H. Guo, D. Xia, Y. Zheng, Y. Zhu, Y. Liu, Y. Zhou, A pure zinc membrane with degradability and osteogenesis promotion for guided bone regeneration: in vitro and in vivo studies, Acta Biomater. 106 (2020) 396–409, https://doi.org/10.1016/j.actbio.2020.02.024. Apr.
[8] R. Gutta, R.A. Baker, A.A. Bartolucci, P.J. Louis, Barrier membranes used for ridge augmentation: is there an optimal pore size? J. Oral Maxillofac. Surg. 67 (6) (2009) 1218–1225, https://doi.org/10.1016/j.joms.2008.11.022. Jun.
[9] Y. Shi, et al., Customized barrier membrane (titanium alloy, poly ether-ether ketone and unsintered hydroxyapatite/poly-L-lactide) for guided bone regeneration, Front. Bioeng. Biotechnol. 10 (2022), https://doi.org/10.3389/fbioe.2022.916967. Jun.
[10] M. Benedetti, A. du Plessis, R.O. Ritchie, M. Dallago, S.M.J. Razavi, F. Berto, Architected cellular materials: a review on their mechanical properties towards fatigue-tolerant design and fabrication, Mater. Sci. Eng. R Rep. 144 (2021), https://doi.org/10.1016/j.mser.2021.100606. Elsevier LtdApr. 01,.
[11] O. Al-Ketan, R. Rowshan, A.H. Alami, Biomimetic materials for engineering applications. Encyclopedia of Smart Materials, Elsevier, 2022, pp. 25–34, https://doi.org/10.1016/B978-0-12-815732-9.00019-X.
[12] B. Niu, J. Yan, A new micromechanical approach of micropolar continuum modeling for 2-D periodic cellular material, Acta Mech. Sin./Lixue Xuebao 32 (3) (2016) 456–468, https://doi.org/10.1007/s10409-015-0492-8. Jun.
[13] S.C. Cowin, J.W. Nunziato, Linear elastic materials with voids, J. Elast. 13 (2) (1983) 125–147, https://doi.org/10.1007/BF00041230. Jul.
[14] L. Leonetti, N. Fantuzzi, P. Trovalusci, F. Tornabene, Scale effects in orthotropic composite assemblies as micropolar continua: a comparison between weakand strong-form finite element solutions, Materials. (Basel) 12 (5) (2019), https://doi.org/10.3390/ma12050758.
[15] L.J. Gibson, M.F. Ashby, Cellular solids, Cambridge University Press, 1997, https://doi.org/10.1017/CBO9781139878326.
[16] S. Liu, W. Su, Effective couple-stress continuum model of cellular solids and size effects analysis, Int. J. Solids. Struct. 46 (14–15) (2009) 2787–2799, https://doi.org/10.1016/j.ijsolstr.2009.03.007. Jul.
[17] M. Colatosti, N. Fantuzzi, P. Trovalusci, R. Masiani, New insights on homogenization for hexagonal-shaped composites as Cosserat continua, Meccanica 57 (4) (2022) 885–904, https://doi.org/10.1007/s11012-021-01355-x. Apr.
[18] V. Sansalone, P. Trovalusci, F. Cleri, Multiscale modeling of materials by a multifield approach: microscopic stress and strain distribution in fiber-matrix composites, Acta Mater. 54 (13) (2006) 3485–3492, https://doi.org/10.1016/j.actamat.2006.03.041. Aug.
[19] K.K. Żur, M. Arefi, J. Kim, J.N. Reddy, Free vibration and buckling analyses of magneto-electro-elastic FGM nanoplates based on nonlocal modified higher-order sinusoidal shear deformation theory, Compos. B Eng. 182 (2020), https://doi.org/10.1016/j.compositesb.2019.107601. Feb.
[20] P. Trovalusci, Molecular Approaches for Multifield Continua: origins and current developments, in: CISM International Centre For Mechanical Sciences, Courses and Lectures, 556, Springer International Publishing, 2014, pp. 211–278, https://doi.org/10.1007/978-3-7091-1812-2_7.
[21] R. Izadi, M. Tuna, P. Trovalusci, E. Ghavanloo, Torsional characteristics of carbon nanotubes: micropolar elasticity models and molecular dynamics simulation, Nanomaterials 11 (2) (2021) 1–20, https://doi.org/10.3390/nano11020453. Feb.
[22] S.A. Faghidian, K.K. Żur, J.N. Reddy, A.J.M. Ferreira, On the wave dispersion in functionally graded porous Timoshenko-Ehrenfest nanobeams based on the higher-order nonlocal gradient elasticity, Compos. Struct. 279 (2022), https://doi.org/10.1016/j.compstruct.2021.114819. Jan.
[23] A.C. Eringen and, J.L. Wegner, Nonlocal continuum field theories, Appl. Mech. Rev. 56 (2) (2003) B20–B22, https://doi.org/10.1115/1.1553434. Mar.
[24] H. Ren, X. Zhuang, T. Rabczuk, A nonlocal operator method for solving partial differential equations, Comput. Methods Appl. Mech. Eng. 358 (2020), https://doi.org/10.1016/j.cma.2019.112621. Jan.
[25] T. Rabczuk, H. Ren, X. Zhuang, A nonlocal operator method for partial differential equations with application to electromagnetic waveguide problem, Comput. Mater. Continua 59 (1) (2019) 31–55, https://doi.org/10.32604/cmc.2019.04567.
[26] A.C. Eringen, Theory of micropolar elasticity. Microcontinuum field theories, Springer New York, New York, NY, 1999, pp. 101–248, https://doi.org/10.1007/978-1-4612-0555-5_5.
[27] G. Capriz, Continua with microstructure, 35, Springer New York, New York, NY, 1989, https://doi.org/10.1007/978-1-4612-3584-2.

[28] Q. Wu, Q. Gao, The symplectic approach for analytical solution of micropolar plane stress problem, Int. J. Solids. Struct. 264 (2023), https://doi.org/10.1016/j.ijsolstr.2022.112095. Mar.
[29] S. Forest, K. Sab, Cosserat overall modeling of heterogeneous materials, Mech. Res. Commun. 25 (4) (1998) 449–454, https://doi.org/10.1016/S0093-6413(98)00059-7. Jul.
[30] M. Tuna, P. Trovalusci, Scale dependent continuum approaches for discontinuous assemblies: 'Explicit' and 'implicit' non-local models, Mech. Res. Commun. 103 (2020), https://doi.org/10.1016/j.mechrescom.2019.103461. Jan.
[31] E. Scarpetta, On the fundamental solutions in micropolar elasticity with voids, Acta Mech. 82 (3–4) (1990) 151–158, https://doi.org/10.1007/BF01173624. Sep.
[32] R. Kumar, T. Kansal, Fundamental solution in the theory of micropolar thermoelastic diffusion with voids, Comput. Appl. Math. 31 (1) (2012) 169–189, https://doi.org/10.1590/S1807-03022012000100009.
[33] M. Ciarletta, A. Scalia, M. Svanadze, Fundamental solution in the theory of micropolar thermoelasticity for materials with voids, J. Therm. Stresses 30 (3) (2007) 213–229, https://doi.org/10.1080/01495730601130901. Jan.
[34] R.S. Lakes, Experimental microelasticity of two porous solids, Int. J. Solids. Struct. 22 (1) (1986) 55–63, https://doi.org/10.1016/0020-7683(86)90103-4.
[35] M. Marin, E. Carrera, A.E. Abouelregal, Structural stability study for porous Cosserat media. Mechanics of Advanced Materials and Structures, 2023, pp. 1–9, https://doi.org/10.1080/15376494.2023.2172239. Feb.
[36] M. Benedetti, A. du Plessis, R.O. Ritchie, M. Dallago, S.M.J. Razavi, F. Berto, Architected cellular materials: a review on their mechanical properties towards fatigue-tolerant design and fabrication, Mater. Sci. Eng. R Rep. 142 (2021), https://doi.org/10.1016/j.mser.2021.100606. Elsevier LtdApr. 01,.
[37] P. Trovalusci, M.L. De Bellis, R. Masiani, A multiscale description of particle composites: from lattice microstructures to micropolar continua, Compos. B Eng. 128 (2017) 164–173, https://doi.org/10.1016/j.compositesb.2017.06.015. Nov.
[38] N. Fantuzzi, P. Trovalusci, R. Luciano, Multiscale analysis of anisotropic materials with hexagonal microstructure as micropolar continua, Int. J. Multiscale Comput. Eng. 18 (2) (2020) 265–284, https://doi.org/10.1615/IntJMultCompEng.2020032920.
[39] N. Fantuzzi, P. Trovalusci, S. Dharasura, Mechanical behavior of anisotropic composite materials as micropolar continua, Front. Mater. 6 (2019), https://doi.org/10.3389/fmats.2019.00059. Apr.
[40] M. Yoder, L. Thompson, J. Summers, Size effects in lattice structures and a comparison to micropolar elasticity, Int. J. Solids. Struct. 143 (2018) 245–261, https://doi.org/10.1016/j.ijsolstr.2018.03.013. Jun.
[41] Y. Maalej, M.I. El Ghezal, I. Doghri, Micromechanical approach for the behaviour of open cell foams, Eur. J. Comput. Mech. 22 (2–4) (2013) 198–208, https://doi.org/10.1080/17797179.2013.820979. Aug.
[42] Z. Rueger, R.S. Lakes, Experimental Cosserat elasticity in open-cell polymer foam, Philos. Mag. 96 (2) (2016) 93–111, https://doi.org/10.1080/14786435.2015.1125541. Jan.
[43] R.S. Lakes, Cosserat shape effects in the bending of foams, Mech. Adv. Mater. Struct. (2022) 1–5, https://doi.org/10.1080/15376494.2022.2086328. Jun.
[44] R. Izadi, M. Tuna, P. Trovalusci, N. Fantuzzi, Bending characteristics of carbon nanotubes: micropolar elasticity models and molecular dynamics simulations, Mech. Adv. Mater. Struct. 30 (1) (2021) 189–206, https://doi.org/10.1080/15376494.2021.2011499.
[45] H. Ramézani, J. Jeong, Z.Q. Feng, On parallel simulation of a new linear Cosserat elasticity model with grid framework model assumptions, Appl. Math. Model. 35 (10) (2011) 4738–4758, https://doi.org/10.1016/j.apm.2011.03.054. Oct.
[46] J. Kim, K.K. Żur, J.N. Reddy, Bending, free vibration, and buckling of modified couples stress-based functionally graded porous micro-plates, Compos. Struct. 209 (2019) 879–888, https://doi.org/10.1016/j.compstruct.2018.11.023. Feb.
[47] P. Jankowski, K.K. Żur, A. Farajpour, Analytical and meshless DQM approaches to free vibration analysis of symmetric FGM porous nanobeams with piezoelectric effect, Eng. Anal. Bound. Elem. 136 (2022) 266–289, https://doi.org/10.1016/j.enganabound.2022.01.007. Mar.
[48] I. Goda, M. Assidi, J.F. Ganghoffer, A 3D elastic micropolar model of vertebral trabecular bone from lattice homogenization of the bone microstructure, Biomech. Model. Mechanobiol. 13 (1) (2014) 53–83, https://doi.org/10.1007/s10237-013-0486-z. Jan.
[49] I. Goda, M. Assidi, S. Belouettar, J.F. Ganghoffer, A micropolar anisotropic constitutive model of cancellous bone from discrete homogenization, J. Mech. Behav. Biomed. Mater. 16 (1) (2012) 87–108, https://doi.org/10.1016/j.jmbbm.2012.07.012.
[50] H.C. Park, R.S. Lakes, Cosserat micromechanics of human bone: strain redistribution by a hydration sensitive constituent, J. Biomech. 19 (5) (1986) 385–397, https://doi.org/10.1016/0021-9290(86)90015-1. Jan.
[51] J.F.C. Yang, R.S. Lakes, Experimental study of micropolar and couple stress elasticity in compact bone in bending, J. Biomech. 15 (2) (1982) 91–98, https://doi.org/10.1016/0021-9290(82)90040-9. Jan..
[52] R. Lakes, J.L. Katz, Bone and teeth, properties of. Encyclopedia of Medical Devices and Instrumentation, John Wiley & Sons, Inc., Hoboken, NJ, USA, 2006, https://doi.org/10.1002/0471732877.emd042.
[53] Z. Rueger, R.S. Lakes, Experimental study of elastic constants of a dense foam with weak cosserat coupling, J. Elast. 137 (1) (2019) 101–115, https://doi.org/10.1007/s10659-018-09714-8. Oct.
[54] J.F.C. Yang, R.S. Lakes, Transient study of couple stress effects in compact bone: torsion, J. Biomech. Eng. 103 (4) (1981) 275–279, https://doi.org/10.1115/1.3138292. Nov.
[55] J. Fatemi, P.R. Onck, G. Poort, F. Van Keulen, Cosserat moduli of anisotropic cancellous bone: a micromechanical analysis, J. Phys. IV (Proceedings) 105 (2003) 273–280, https://doi.org/10.1051/jp4:20030197. Mar.
[56] R.S. Lakes, Experimental evaluation of micromorphic elastic constants in foams and lattices, Z. Angew. Math. Phys. 74 (1) (2023), https://doi.org/10.1007/s00033-022-01923-5. Feb.
[57] P. Trovalusci, A. Pau, Derivation of microstructured continua from lattice systems via principle of virtual works: the case of masonry-like materials as micropolar, second gradient and classical continua, Acta Mech. 225 (1) (2014) 157–177, https://doi.org/10.1007/s00707-013-0936-9. Jan.
[58] S. Ramalingam, C. Sundar, J.A. Jansen, H. Alghamdi, Alveolar bone science: structural characteristics and pathological changes. Dental Implants and Bone Grafts, Elsevier, 2020, pp. 1–22, https://doi.org/10.1016/B978-0-08-102478-2.00001-5.
[59] K. Gulabivala, Y.L. Ng, Tooth organogenesis, morphology and physiology. Endodontics, Elsevier, 2014, pp. 2–32, https://doi.org/10.1016/B978-0-7020-3155-7.00001-1.
[60] L. Bai, P. Ji, X. Li, H. Gao, L. Li, C. Wang, Mechanical characterization of 3D-printed individualized Ti-Mesh (Membrane) for Alveolar Bone Defects, J. Healthc. Eng. 2019 (2019) 4231872, https://doi.org/10.1155/2019/4231872.
[61] N. Fantuzzi, P. Trovalusci, R. Luciano, Material symmetries in homogenized hexagonal-shaped composites as cosserat continua, Symmetry. (Basel) 12 (3) (2020), https://doi.org/10.3390/sym12030441. Mar.
[62] P. Trovalusci, R. Masiani, Material symmetries of micropolar continua equivalent to lattices, Int. J. Solids. Struct. 36 (14) (1999) 2091–2108, https://doi.org/10.1016/S0020-7683(98)00073-0. May.
[63] R. Lakes, W.J. Drugan, Bending of a Cosserat elastic bar of square cross section: theory and experiment, J. Appl. Mech. 82 (9) (2015), https://doi.org/10.1115/1.4030626. Sep.
[64] M. Tuna, L. Leonetti, P. Trovalusci, and M. Kirca, '"Explicit' and 'implicit' non-local continuum descriptions: plate with circular hole," 2021, pp. 311–338. 10.1007/978-3-030-63050-8_11.
[65] M. Sokolowski, Theory of couple-stresses in bodies with constrained rotations: course held at the department for mechanics of deformable bodies July 1970. CISM International Centre For Mechanical Sciences, Springer Vienna, 1980 [Online]. Available: https://books.google.it/books?id=-TOezQEACAAJ.
[66] M.L. De Bellis, D. Addessi, A cosserat based multi-scale model for masonry structures,, Int. J. Multiscale Comput. Eng. 9 (5) (2011) 543–563, https://doi.org/10.1615/IntJMultCompEng.2011002758.
[67] S.E. Alavi, J.F. Ganghoffer, M. Sadighi, Chiral Cosserat homogenized constitutive models of architected media based on micromorphic homogenization, Math. Mech. Solids 27 (10) (2022) 2287–2313, https://doi.org/10.1177/10812865221106941. Oct.

[68] S.E. Alavi, M. Nasimsobhan, J.F. Ganghoffer, A. Sinoimeri, M. Sadighi, Chiral Cosserat model for architected materials constructed by homogenization, Meccanica 56 (10) (2021) 2547–2574, https://doi.org/10.1007/s11012-021-01381-9. Oct.
[69] S.E. Alavi, J.F. Ganghoffer, H. Reda, M. Sadighi, Construction of micromorphic continua by homogenization based on variational principles, J. Mech. Phys. Solids. 153 (2021), https://doi.org/10.1016/j.jmps.2020.104278. Aug.
[70] S.E. Alavi, J.F. Ganghoffer, M. Sadighi, M. Nasimsobhan, A.H. Akbarzadeh, Continualization method of lattice materials and analysis of size effects revisited based on Cosserat models, Int. J. Solids. Struct. 254–255 (2022), https://doi.org/10.1016/j.ijsolstr.2022.111894. Nov.
[71] H. Reda, S.E. Alavi, M. Nasimsobhan, J.F. Ganghoffer, Homogenization towards chiral Cosserat continua and applications to enhanced Timoshenko beam theories, Mech. Mater. 155 (2021), https://doi.org/10.1016/j.mechmat.2020.103728. Apr.
[72] P.M. Mariano, P. Trovalusci, Constitutive relations for elastic microcracked bodies: from a lattice model to a multifield continuum description, Int. J. Damage Mech. 8 (2) (1999) 153–173, https://doi.org/10.1177/105678959900800204. Apr.
[73] E. Providas, M.A. Kattis, Finite element method in plane Cosserat elasticity, Comput. Struct. 80 (27–30) (2002) 2059–2069, https://doi.org/10.1016/S0045-7949(02)00262-6. Nov.
[74] M. Hodaei, P. Maghoul, N. Wu, Three-dimensional biomechanical modeling of cylindrical bone-like porous materials subject to acoustic waves, Int. J. Mech. Sci. 213 (2022), https://doi.org/10.1016/j.ijmecsci.2021.106835. Jan.
[75] Z. Cui, Y. Huang, H. Liu, Predicting the mechanical properties of brittle porous materials with various porosity and pore sizes, J. Mech. Behav. Biomed. Mater. 71 (2017) 10–22, https://doi.org/10.1016/j.jmbbm.2017.02.014. Jul.
[76] I. Zein, D.W. Hutmacher, K.C. Tan, S.H. Teoh, Fused deposition modeling of novel scaffold architectures for tissue engineering applications, Biomaterials 23 (4) (2002) 1169–1185, https://doi.org/10.1016/S0142-9612(01)00232-0. Feb.
[77] R. Singh, et al., Characterization of the deformation behavior of intermediate porosity interconnected Ti foams using micro-computed tomography and direct finite element modeling, Acta Biomater. 6 (6) (2010) 2342–2351, https://doi.org/10.1016/j.actbio.2009.11.032.
[78] Y. Zhao, Y. Wang, J. Hao, Y. Wang, K. Wang, S. Tai, Study on mechanical properties of cellular structures with negative Poisson's ratio based on the development of Abaqus plug-in tool, Compos. Struct. 322 (2023), https://doi.org/10.1016/j.compstruct.2023.117348. Oct.
[79] V.A. Eremeyev, A. Skrzat, A. Vinakurava, Application of the micropolar theory to the strength analysis of bioceramic materials for bone reconstruction, Strength Mater. 48 (4) (2016) 573–582, https://doi.org/10.1007/s11223-016-9800-1. Jul.
[80] V.A. Eremeyev, A. Skrzat, F. Stachowicz, Linear micropolar elasticity analysis of stresses in bones under static loads, Strength Mater. 49 (4) (2017) 575–585, https://doi.org/10.1007/s11223-017-9901-5. Jul.
[81] S. Van Bael, et al., The effect of pore geometry on the in vitro biological behavior of human periosteum-derived cells seeded on selective laser-melted Ti6Al4V bone scaffolds, Acta Biomater. 8 (7) (2012) 2824–2834, https://doi.org/10.1016/j.actbio.2012.04.001.
[82] N. Abbasi, S. Hamlet, R.M. Love, N.T. Nguyen, Porous scaffolds for bone regeneration, J. Sci. Adv. Mater. Dev. 5 (1) (2020) 1–9, https://doi.org/10.1016/j.jsamd.2020.01.007. Elsevier B.V.Mar. 01,.
[83] R. Izadi, M. Tuna, P. Trovalusci, N. Fantuzzi, Thermomechanical characteristics of green nanofibers made from polylactic acid: an insight into tensile behavior via molecular dynamics simulation, Mech. Mater. 181 (2023), https://doi.org/10.1016/j.mechmat.2023.104640. Jun.
[84] R. Izadi, P. Trovalusci, N. Fantuzzi, A study on the effect of doping metallic nanoparticles on fracture properties of polylactic acid nanofibres via molecular dynamics simulation, Nanomaterials 13 (6) (2023) 989, https://doi.org/10.3390/nano13060989. Mar.
[85] L. Wang, et al., Microcell morphology evolution and mechanical performance of UHMWPE/PEG porous materials with bimodal cell structure, Compos. Struct. 322 (2023), https://doi.org/10.1016/j.compstruct.2023.117347. Oct.
[86] A. Najibi, T. Mokhtari, Functionally graded materials for knee and hip arthroplasty; an update on design, optimization, and manufacturing, Compos. Struct. 322 (2023), https://doi.org/10.1016/j.compstruct.2023.117350. Elsevier LtdOct. 15,.
[87] Z. Liu, H. Gong, J. Gao, L. Liu, Bio-inspired design, mechanical and mass-transport characterizations of orthotropic TPMS-based scaffold, Compos. Struct. 321 (2023), https://doi.org/10.1016/j.compstruct.2023.117256. Oct.
[88] M. Fan, et al., Microstructure design and mechanical properties of 3D printed graded lattice sandwich structures with tailored porosity, Compos. Struct. 321 (2023), https://doi.org/10.1016/j.compstruct.2023.117323. Oct.
[89] H. Li, B. Yao, Z. Li, Y. Peng, H. Fan, Compressive properties and deformation mechanism of selective laser melting of Ti6Al4V porous femoral implants based on topological optimization, Compos. Struct. 321 (2023), https://doi.org/10.1016/j.compstruct.2023.117326. Oct.
[90] N. Mawassy, J.F. Ganghoffer, H. Reda, S.E. Alavi, H. Lakiss, Analysis of surface effects based on first and second strain gradient mechanics, Mech. Mater. 175 (2022), https://doi.org/10.1016/j.mechmat.2022.104462. Dec.
[91] F.R. Verri, et al., Three-dimensional finite element analysis of anterior single implant-supported prostheses with different bone anchorages, Sci. World J. 2015 (2015), https://doi.org/10.1155/2015/321528.
[92] H. Lu, T.U. Lee, J. Ma, D. Chen, Y.M. Xie, Designing 2D stochastic porous structures using topology optimisation, Compos. Struct. 321 (2023), https://doi.org/10.1016/j.compstruct.2023.117305. Oct.